

Magnetodynamical response of large-area close-packed arrays of circular dots fabricated by nanosphere lithography

E. K. Semenova,¹ F. Montoncello,² S. Tacchi,^{3,6} G. Dürr,⁴ E. Sirotkin,⁵ E. Ahmad,⁵ M. Madami,³ G. Gubbiotti,^{3,6} S. Neusser,⁴ D. Grundler,⁴ F. Y. Ogrin,⁵ R. J. Hicken,⁵ V. V. Kruglyak,⁵ D. V. Berkov,^{1,*} N. L. Gorn,¹ and L. Giovannini²

¹*Innovent Technology Development, Pruessingstr. 27B, D-07749, Jena, Germany*

²*Dipartimento di Fisica, CNISM-University of Ferrara, Via G. Saragat 1, I-44100 Ferrara, Italy*

³*CNISM and Dipartimento di Fisica, University of Perugia, Via A. Pascoli, I-06123 Perugia, Italy*

⁴*Physik Department E10, Technische Universität München, James-Frank-Str., D-85748 Garching, Germany*

⁵*School of Physics, University of Exeter, Stocker road, Exeter, EX4 4QL, United Kingdom*

⁶*Istituto Officina dei Materiali del Consiglio Nazionale delle Ricerche (IOM-CNR), Sede di Perugia, c/o Dipartimento di Fisica, Via A. Pascoli, I-06123 Perugia, Italy*

(Received 25 June 2012; revised manuscript received 22 March 2013; published 28 May 2013)

We report a combined experimental and theoretical study of the quasistatic hysteresis and dynamic excitations in large-area arrays of NiFe nanodisks forming a hexagonal lattice with the lattice constant of 390 nm. Arrays were fabricated by patterning a 20-nm-thick NiFe film using the etched nanosphere lithography. We have studied a close-packed (edge-to-edge separation between disks $d_{cp} = 65$ nm) and an ultraclose packed ($d_{ucp} = 20$ nm) array. Hysteresis loops for both arrays were qualitatively similar and nearly isotropic, i.e., independent on the in-plane external field orientation. The shape of these loops revealed that magnetization reversal is governed by the formation and expulsion of vortices inside the nanodisks. When we assumed that the nanodisks' magnetization significantly decreases near their edges, micromagnetic simulations with material parameters determined independently from continuous film measurements could satisfactorily reproduce the hysteresis. Despite the isotropic hysteresis, significant in-plane anisotropy of the dynamic response of the ultraclose-packed array was found experimentally by the all-electrical spin-wave spectroscopy and Brillouin light scattering. Dynamical simulations could successfully reproduce the difference between excitation spectra for fields directed along the two main symmetry axes of the hexagonal lattice. Simulations revealed that this difference is caused by the magnetodipolar interaction between nanodisks, which leads to a strong variation of the spatial distribution of the oscillation power both for bulk and edge modes as a function of the bias field orientation. Comparison of simulated and measured frequencies enabled the unambiguous identification of experimentally observed modes. Results of this systematic research are relevant both for fundamental studies of spin-wave modes in patterned magnetic structures and for the design of magnonic crystals for potential applications as, e.g., spin-wave guides and filters.

DOI: [10.1103/PhysRevB.87.174432](https://doi.org/10.1103/PhysRevB.87.174432)

PACS number(s): 75.75.Jn, 75.75.Cd, 75.78.Cd

I. INTRODUCTION

The confinement and quantization of spin waves¹ in one (1D) and two (2D) dimensional nano- and microscale magnetic elements have recently become the focal point of intense research.^{2–12} Furthermore, the renaissance of interest to magnonic crystals^{13,14}—media with periodic modulation of magnetic parameters—has led to several important advances in the understanding of propagation, confinement, and quantization of spin waves in magnetostatically coupled 1D^{15–17} and 2D^{18–21} arrays of magnetic elements and 2D arrays of antidots (holes in continuous films).^{22,23} As a result, magnonics²⁴ has emerged as a field aiming at investigation of propagating spin waves in nanostructured magnetic samples, with a promise of reprogrammable artificial crystals¹⁷ and magnetic logic gates,²⁵ magnetoelectronic devices,²⁶ and metamaterials.²⁷

The application of nanostructured magnetic arrays in the electromagnetic metamaterials domain requires the fabrication of samples with sizes either comparable to or greater than the electromagnetic wavelength at the frequency of interest. The fabrication of mm-to-cm scale (corresponding to GHz frequency range) periodic structures consisting of (or containing) magnetic materials precisely and controllably tailored

at the nanometer scale is a major technological challenge, even beyond the context of nanoscale magnonics.²⁸ This challenge is at the limit of current lithographic tools so that bottom-up technologies are explored as possible alternatives. Such large-area patterned arrays form the basis of several types of magnetic recording technology, e.g., bit patterned media and magnetic random access memory arrays, operated at increasingly high data rates. Such structures are necessary also to study the propagation of collective excitations over relatively long distances and to increase the signal-to-noise ratio in magnetic measurements.

Under such circumstances, the etched nanosphere lithography (ENSL) has proved itself as a cost-effective and versatile mean for the demanding magnetic nanofabrication tasks.²⁹ The recent dynamical studies of large-area hexagonal arrays of magnetic nanoelements fabricated by the ENSL have demonstrated their high structural and magnetic quality.^{30,31} However, the sensitivity of these studies was insufficient to confirm and to study the magnetodynamic effects observed in arrays of elements formed by more established lithographical tools.^{27,32,33} Dynamical properties of close-packed square arrays of circular dots in the saturated ground state have been experimentally investigated either by ferromagnetic resonance

(FMR)^{34–36} or by Brillouin light scattering (BLS).^{37–39} On the contrary, arrays of circular magnetic nanoelements (nanodisks) arranged into a hexagonal lattice have been so far less investigated. Such arrays, representing one of the basic 2D crystallographic lattice types, are highly interesting both from the fundamental point of view (studies of the influence of the in-plane anisotropy of the magnetodipolar interaction on the spin-wave spectra of such arrays) and for exploiting different applications of magnonic crystals (where the structure of magnonic bands depends on the interelement distance and arrangement).

Theoretical analysis of the magnetization dynamics in arrays of thin magnetic nanoelements is highly complicated both due to the long-range character of the magnetodipolar interaction and the possibly inhomogeneous magnetization ground state of such nanoelements. Neglecting the latter complication (i.e., assuming that all elements are in a magnetically saturated state), corresponding theoretical description of the spin-wave spectrum could be developed for 2D and 3D arrays of spherical particles⁴⁰ and 2D arrays of thin-film elements having a rectangular lateral shape.⁴¹ The semianalytical approach developed in Ref. 42 for the calculation of the spin-wave spectrum for a 2D array of magnetic nanoelements can be in principle generalized to a system with a nonsaturated ground state of these nanoelements. The frequency splitting of normal modes of magnetic elements due to the magnetodipolar interaction with their neighbors can be calculated using the perturbation method from Ref. 43. The method relies, however, on a fairly strong assumption that the mode character within individual elements remains unaltered by the interaction.

Keeping in mind that in most fundamentally interesting and practically relevant cases the size of nano-elements in such arrays is far above the critical single-domain size, calculations of their dynamical properties have to take into account a nontrivial magnetization structure of their ground states. This task obviously requires the application of numerical methods, which at present can be roughly divided into so-called dynamical matrix methods (DMMs) and classical micromagnetic simulations. In the former methods, the equations of motion for magnetic moments (usually the Landau-Lifshitz equations) of a discretized system under study are linearized with respect to the small deviations of these magnetic moments from the equilibrium state.⁴⁴ Application of this method to the nanoparticles arrays requires the implementation of periodic boundary conditions (PBCs). The corresponding extension of DMM has been developed in Ref. 45, where the method was applied to a rectangular lattice of circular nanodots.

Full-scale micromagnetic simulations solve the Landau-Lifshitz equations of motion in the time domain. The time Fourier transform is then applied to the trajectories of magnetic moments, thus allowing one to obtain the corresponding power-oscillation spectrum for the whole array, including the spatial distribution of the oscillation power within the array nanoelements. Unfortunately, in most micromagnetic codes, periodic in-plane boundary conditions are not implemented. Hence, the researchers are forced to compute the magnetization response of finite arrays of nanoelements, making these arrays as large as possible in the hope to gain the insights into the behavior of macroscopically large periodic

arrays from the spin-wave spectra obtained for the central elements of simulated relatively small systems. This way the arrays of nanodisks and square-shaped nanoelements on a square lattice with the maximal size of 10×10 elements were analyzed (see, e.g., Refs. 11, 19, 27, 33, 46, 47, and 48). Numerical studies of nanoarrays using micromagnetic simulations with properly implemented PBCs and simulation results for magnetization dynamics of hexagonal arrays of nanoelements are, to our knowledge, virtually absent. We note in passing that magnetization dynamics of hexagonally ordered antidots—i.e., holes in a continuous film—were studied analytically and numerically,⁴⁹ with emphasis on the reasons for the anisotropic FMR response of such a system.

In the present work, we investigate in detail quasistatic magnetization reversal and magnetodynamical properties of closely packed arrays of circular dots fabricated by ENSL. We combine experimental measurements performed using the magneto-optical Kerr effect (MOKE), all-electrical spin-wave spectroscopy (AESWS) and BLS with numerical studies carried out by full-scale micromagnetic simulations and the DMM, whereby both numerical methods use true PBCs. The rigorous theoretical analysis applied to high-quality experimental data allow us to achieve a deep understanding of the factors governing the evolution of the excitation spectra caused by the variation of the magnitude and orientation of the external magnetic field. The analysis highlights the variation of the spatial localization of normal modes within individual elements, thereby emphasizing the importance of the presented micromagnetic approach for correct interpretation of spin waves in magnonic crystals.

The paper is organized as follows. In Sec. II, we introduce in detail our fabrication and characterization techniques, providing structural parameters of the hexagonal nanodisk arrays studied here. Afterward, we briefly remember the basics of experimental methods used for the static (MOKE) and dynamic (AESWS and BLS) measurements in this work. Section III A contains results of hysteresis loop measurements and their comparison with corresponding numerical simulations. Experimental results on the magnetization dynamics, obtained using AESWS and BLS, are compared in Sec. III B. The next part, Sec. III C, is devoted to the theoretical analysis of the arrays under study performed by two kinds of numerical simulations—DMM and full-scale micromagnetic simulations. First, in Sec. III C 1, we study the case when the external field is directed perpendicular to the disk rows of the hexagonal lattice. We begin this study with the comparison of simulation results obtained by both numerical methods for the array of disks with ideally sharp edges in order to demonstrate the reliability of our numerical analysis. Next, we study the effect of the edge imperfection on the eigenmode spectrum obtained by spatially homogeneous excitations (modes visible in AESWS experiments) and modes excited by field pulses with various spatial symmetries (i.e., modes which might be detected both by the AESWS and BLS techniques). In Sec. III C 2, we repeat this analysis for the case of the external field directed parallel to the disk rows, emphasizing the differences arising from the change of the field orientation. We finish our discussion with the comparison between theoretical and numerical results, which enables us to identify which spin

wave modes have been observed experimentally. Our major findings are summarized in Sec. IV.

II. SAMPLE FABRICATION AND EXPERIMENTAL METHODOLOGY

A. Fabrication and characterization via scanning electron microscopy

Two arrays of $\text{Ni}_{80}\text{Fe}_{20}$ (Py) nanodisk arranged into a hexagonal lattice (Fig. 1) were prepared using ENSL. To fabricate the arrays of nanoelements, a nominally 20-nm-thick polycrystalline Py film with a 3-nm-thick cap of Si_3N_4 was magnetron sputtered onto a GaAs substrate. A close-packed monolayer of polystyrene spheres of 390-nm diameter self-assembled on the water-air interface was carefully transferred onto the film surface. The spheres on the magnetic film were then etched in oxygen plasma to reduce their diameter while preserving the center-to-center separation (the lattice period). Following the oxygen etching, the array of etched spheres was used as a mask in the argon ion-milling process. The pattern formed by the spheres was thereby transferred into the magnetic film and used to mill the film through its entire thickness. Finally, the spheres were removed, and the patterned film was covered by an additional 7-nm-thick cap of Si_3N_4 in order to prevent the exposed magnetic disk edges from oxidation. The details of the ENSL technique and the optimized conditions for large-area fabrication are described elsewhere.^{29,50}

Both samples were inspected under a scanning electron microscope (SEM) to quantify any variations in the element size and the period and orientation of the symmetry axes of the arrays over their entire area. The SEM images were acquired from 32 sites forming an 8×4 array with a 0.5-mm period, therefore evenly covering the entire rectangular samples of $5.6 \times 2.6 \text{ mm}^2$ size. In Fig. 1, we define relevant geometrical parameters that were extracted from measurements.

In the first sample, the average diameter of the disks was found to be $325 (\pm 2) \text{ nm}$, with no significant variation observed

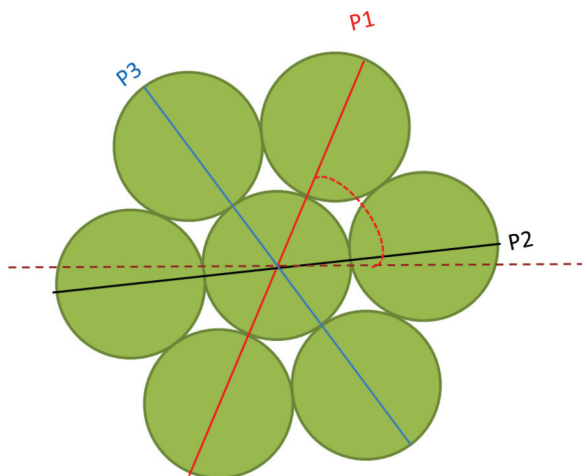


FIG. 1. (Color online) The different symmetry axes (P1, P2, and P3) of the array are schematically shown. The orientation of the axes was defined by the angles that they formed with respect to an edge of the substrate indicated by the dotted line.

over the whole sample area. In the center of the sample, the P1 symmetry axis (Fig. 1) forms an average angle of 70° relative to the edge parallel to the sample's length. However, a gradual decrease of this value from 56° to 78° was observed along the length of the sample. The two extremes fall near the two edges along the length; therefore, they could not influence the data. A perfect hexagonal symmetry would result in an angular separation of 60° between the symmetry axes. In the sample, the average angles between axes P1 and P2, P2 and P3, and P3 and P1 were observed to be 60° , 58.5° , and 61.5° , respectively, indicating a very good long-range ordering. Periodicity of the sample along the P3 axis was close to 390 nm (i.e., equal to the center-to-center separation between neighboring nanospheres, as expected), whereas the periodicities along the other two axes varied. Periods along P1 and P2 were observed to be about 385 nm and about 395 nm, respectively, yet yielding the overall accuracy in the period of nearly 1%. The edge-to-edge separation between elements within the array was therefore $65 (\pm 5) \text{ nm}$. In the following, the sample is referred to as the close-packed array (*cp* array).

In the second sample, the average disk diameter was found to be $378 (\pm 2) \text{ nm}$. In the center of the sample, the P1 symmetry axis forms an average angle of 40° relative to the sample's long edge. The orientation of this axis suffers a decrease of 25° over the distance of 5.0 mm. The maximum of 45° is observed at one end and the minimum of 20° is observed on the other end of the sample. The rate of this variation was observed to be greater near the ends and much smaller near the center of the sample, with the latter portion of the sample providing the major contribution to the measurements described below. The periods along the P1, P2, and P3 axes are $392 (\pm 6) \text{ nm}$, $395 (\pm 1) \text{ nm}$, and $384 (\pm 2) \text{ nm}$, respectively. The average edge-to-edge separation between elements within the array was therefore $12 (\pm 5) \text{ nm}$. Only the average angle between P1 and P2 was measured for this sample to yield $58 (\pm 1)$ degrees. We shall refer to this sample as the ultraclose-packed array (*ucp* array).

It is useful also to introduce the standard Bravais-Miller indices $[h, k, i, l]$ for hexagonal systems to address the relevant directions in the direct space. We omit the fourth index l , because in our 2D planar array it is always zero. The principal in-plane directions are hence characterized by the triad $[h, k, i]$. In particular, the direction along the nanodisk rows (x direction in Fig. 2, with $\phi = 90^\circ$) corresponds to the indices

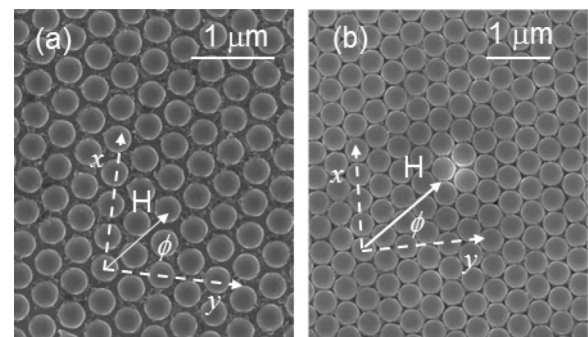


FIG. 2. Representative SEM images of (a) *cp* and (b) *ucp* arrays; here ϕ denotes the angle between the in-plane bias field \mathbf{H} and the in-plane direction perpendicular to the nanodisk rows.

$[2, -1, -1]$, while the direction perpendicular to the nanodisk rows (y direction in Fig. 2, with $\phi = 0^\circ$) is the $[0, -1, 1]$ direction.

B. Experimental techniques for the static and dynamic magnetic characterization

Magnetic hysteresis loops were measured for both the *cp* and *ucp* arrays using a conventional MOKE apparatus based on a photoelastic modulator and a lock-in amplifier, working in a longitudinal magneto-optical configuration (i.e., with the external field applied parallel to the sample surface and to the plane of incidence of light). In this configuration, the signal collected from a photodiode is proportional to the in-plane component of the magnetization parallel to the applied field.

Spectra of magnetic spin excitations were measured by AESWS and BLS techniques. In this work, AESWS measures the resonant dynamic response of a magnetic system excited by an rf field,⁵¹ while BLS is used for detecting thermally excited spin waves. In the AESWS experiments, a vector network analyzer (VNA) connected to a $50\ \Omega$ matched coplanar waveguide (CPW) served both as the source and the detector of spin waves in the sample placed face-down onto the CPW. The inner conductor of the CPW had a width $w = 20\ \mu\text{m}$ and a length $L = 9\ \text{mm}$. The CPW excited a broad spectrum of wave vectors with a maximum value of about $\pi/2w \approx 0.8 \times 10^3\ \text{rad/cm}$, i.e., the long-wave excitations were probed. The output power of the VNA was $-5\ \text{dBm}$. For measuring resonant excitations, the external static magnetic field \mathbf{H} was applied under different rotation angles ϕ . Note that the spectra reported here have been obtained by subtracting a reference spectrum where \mathbf{H} was applied perpendicular to the CPW. By this difference technique, we increased the signal-to-noise ratio.⁵²

BLS experiments were performed in the backscattering configuration using the green light (wavelength $\lambda = 532\ \text{nm}$) of a single-mode diode-pumped solid-state laser and a Sandercock type (3 + 3)-pass tandem Fabry–Perot interferometer.⁵³ A magnetic bias field \mathbf{H} in the range $-1000\ \text{Oe} < H < 1000\ \text{Oe}$ was applied in the sample plane and perpendicular to the plane of light incidence. The sample was mounted on a goniometer, which allows rotation of the sample around its normal direction so that BLS spectra can be recorded for different orientations of \mathbf{H} with respect to the high symmetry directions of the disks array. In order to directly compare frequencies measured by the BLS and AESWS techniques, the angle of light incidence was normal to the sample plane, so that spin waves with a zero Bloch wave vector were probed. However, due to the finite collection angle of the scattered light [numerical aperture (NA) = 0.24], even modes with antisymmetric spatial character can have a nonzero cross section in the scattering process, thereby contributing to the BLS spectra.

C. Numerical simulations methodology

1. Choice of the simulation parameters

Simulation of hysteresis loops was performed using the MicroMagus package.⁵⁴ For both hexagonally arranged *cp* and *ucp* arrays, we have assumed the nanodisk thicknesses $h = 20\ \text{nm}$. On the basis of the SEM analysis (see above),

we have used the center-to-center separation between disks for both samples $L_c = 390\ \text{nm}$, while the disk diameters were chosen to be $D_1 = 325\ \text{nm}$ and $D_2 = 370\ \text{nm}$ for the *cp* and the *ucp* array, respectively; therefore, the edge-to-edge interdisk separation Δl in the *ucp* sample ($\Delta l = 20\ \text{nm}$) was equal to the nanodisk thickness and significantly smaller than for the *cp* array ($\Delta l = 65\ \text{nm}$). Magnetic parameters used in simulations have been obtained by a careful fitting of analytically calculated frequencies of perpendicular standing spin-wave and Damon-Eshbach (DE) modes for a thin film⁵⁵ to the frequencies measured by BLS on the corresponding unpatterned Py film with the same thickness: magnetization $M_S = 715\ \text{erg/cm}^3$, surface out-of-plane anisotropy $K_S = 0.6\ \text{erg/cm}^2$, exchange stiffness $A = 1.0 \times 10^{-6}\ \text{erg/cm}$, and the g factor $g = 2.1$. The magnetocrystalline anisotropy of Py-type alloys is known to be very small. Therefore, we assumed that the film had a polycrystalline structure with the average grain size $\langle d_{\text{gr}} \rangle = 10\ \text{nm}$,^{56,57} the cubic anisotropy constant $K = 5 \times 10^3\ \text{erg/cm}^3$, and a random 3D distribution of grain anisotropy axes. The only result of such a small anisotropy is the elimination of the spatial degeneracy of our problem, which could produce numerical artifacts. The simulation area comprised the elementary cell of the hexagonal lattice with lateral size $390 \times 682\ \text{nm}^2$, containing two nanodisks. It was discretized laterally into 80×140 rectangular discretization cells. No discretization perpendicular to the lattice plane was performed, so that the discretization cells' height was equal to the film thickness $h = 20\ \text{nm}$. Simulations have been done for two orientations of the applied field \mathbf{H} : $[0, -1, 1]$ and $[2, -1, -1]$ directions. To be more precise, the directions were almost perpendicular ($\phi = 2^\circ$) and almost parallel ($\phi = 88^\circ$) to the nanodisk rows; a small 2° field deviation from the main axes was used to avoid the artificial spatial degeneracy mentioned above.

2. Simulation methodology for spin-wave excitations

In micromagnetic simulations, dynamical response of a system is evaluated by numerical solution of the Landau-Lifshitz-Gilbert (LLG) equation of motion for the magnetization $\mathbf{M}(r)$:

$$\frac{d\mathbf{M}}{dt} = -\gamma \cdot [\mathbf{M} \times \mathbf{H}^{\text{eff}}] - \lambda \cdot \frac{\gamma}{M_S} \cdot [\mathbf{M} \times [\mathbf{M} \times \mathbf{H}^{\text{eff}}]], \quad (1)$$

where γ is the gyromagnetic ratio and λ is the Gilbert dissipation constant. The effective field \mathbf{H}_{eff} contains the magnetocrystalline anisotropy, exchange, and magnetodipolar interaction fields. To compute the spin-wave frequencies, we have to calculate the dynamical response of the system to a weak oscillating field, superimposed by a constant field \mathbf{H} . This response is modeled using Eq. (1) with the so-called field-pulse method. In this method, we first find the equilibrium magnetization state in the given constant field \mathbf{H} . Then we apply to the system a short trapezoidal field pulse $\Delta\mathbf{h}(t)$, where the field $\Delta\mathbf{h}$ is directed perpendicular to the sample plane. The rise and fall times of this pulse are sufficiently small (0.05 ns), so that its Fourier spectrum contains significant power up to the highest frequency for which the relevant system eigenmodes are expected. We simulate the system response to this pulse, setting the damping in Eq. (1) to zero ($\lambda = 0$), so that the

magnetization oscillations continue indefinitely after the pulse is switched off.

In order to reproduce all modes observed experimentally in these simulations, field pulses of different spatial symmetries are used. In AESWS, modes are excited by an external field, which is homogeneous on the nanodisk length scale; therefore, to reproduce the AESWS results, we employ the spatially homogeneous pulse $\Delta\mathbf{h}(t)$. On the contrary, spin waves observed in BLS are thermally excited, i.e., they may have any spatial structure with arbitrary phase relations between oscillating regions within one nanodisk. Some of these modes—namely those with nodal lines perpendicular to the bias field \mathbf{H} —may be also excited by a spatially homogeneous pulse due to the presence of a spatially nonhomogeneous magnetodipolar (self-demagnetizing) field directed roughly opposite to \mathbf{H} . In accordance with the commonly accepted classification, we shall refer to these excitations as BA-like (backward volume) modes. However, in order to efficiently excite modes with nodal lines parallel to \mathbf{H} , which we shall call DE-like modes, we have to apply a spatially nonhomogeneous field pulse with one or more nodal lines parallel to \mathbf{H} ; this is especially true for simulations employing PBCs. Hence, to obtain all the modes observed by the BLS technique, we have to use spatially nonhomogeneous pulses. We have chosen pulses directed perpendicular to the layer plane and having the spatial dependence $h_{\perp}(\mathbf{r}, t) = h_0(t) \cdot \sin(\pi n_x x/L_x) \cdot \sin(\pi n_y y/L_y)$. Here $n_x = n_y = 1$ corresponds to the excitation without node lines, thus having the same symmetry as the homogeneous pulse. The pulse with $n_x = 2$ and $n_y = 1$ excites modes with one nodal line parallel to the x axis, etc.

To compute the eigenfrequencies of our system using the DMM, the equilibrium magnetization state was computed using the static part of the MicroMagus package. Then, evaluation of the eigenfrequencies was performed by the DMM software with implemented PBCs.⁴⁵ The same geometry, external field directions, and material parameters as for micromagnetic simulations described above have been used (except that the random grain anisotropy of Py was completely neglected). In contrast to micromagnetic simulations employing Eq. (1), in DMM all spin-wave modes of the system are obtained simultaneously as eigenvectors of a matrix, whose elements

are related to the torque acting on the magnetization in each micromagnetic cell.⁴⁴

III. RESULTS AND DISCUSSION

A. Quasistatic hysteresis: Experimental results and numerical simulations

Hysteresis loops measured in magnetic fields \mathbf{H} applied along the principal symmetry directions of the hexagonal lattice are shown in Fig. 3. Loops of both the cp [Fig. 3(a)] and ucp arrays [Fig. 3(b)] are typical for the vortex formation within individual nanoelements having elliptical or circular in-plane shapes^{58–62} (it was also shown,⁶³ that the magnetization of noninteracting nanodisks with the thickness $h = 20$ nm and diameters between 250 and 400 nm reverses only via the vortex nucleation). For this type of the magnetization switching, when the magnetic field decreases from the positive saturation $M = +M_S$, disks retain their full moment up to approximately zero field at which a sudden decrease of M occurs. This rapid change corresponds to the nucleation of a single vortex, with its core located close to the disk center. When the field decreases further, the vortex gradually moves toward the disk edge, and the magnetization progressively reappears. Finally, when the vortex is expelled out of the disk, the negative saturation is reached by another sharp drop at some critical negative field. In our case, the vortex expulsion occurs at the fields $H_{\text{exp}}^{\text{cp}} \approx 420$ Oe and $H_{\text{exp}}^{\text{ucp}} \approx 300$ Oe for the cp and ucp arrays, respectively. Interestingly, quasistatic loops for both samples show a nearly in-plane isotropic behavior. This indicates that the in-plane anisotropy of the magnetodipolar interdot coupling does not affect significantly the magnetization reversal process. In particular, the reason for a small angular anisotropy of the vortex annihilation field might be a relatively weak stray field produced by the nanodisk edge in a closed (vortex) magnetization configuration of an individual nanodisk.

Our results can be compared to configurational anisotropies measured on arrays of circular disks arranged on a square lattice.^{64,65} For example, the angular anisotropy of the vortex nucleation and annihilation field was found also to be very

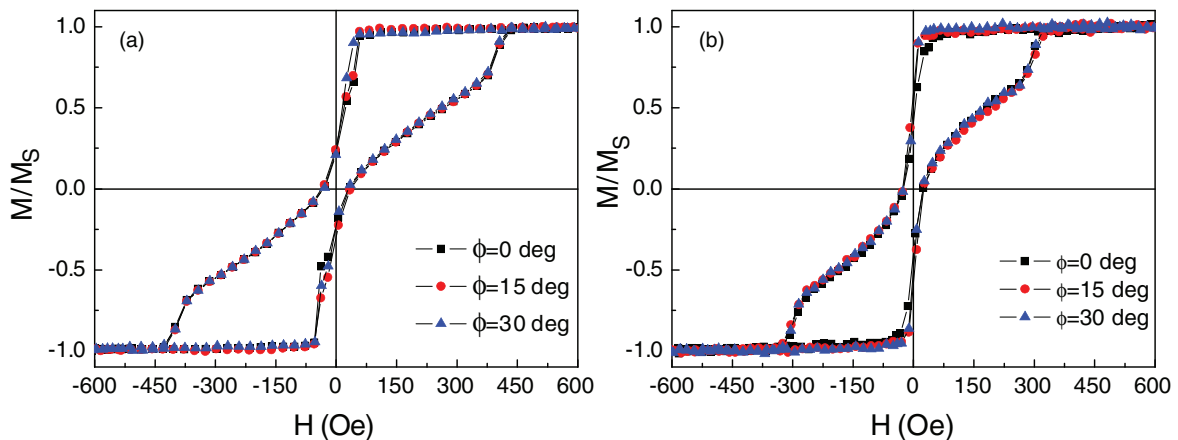


FIG. 3. (Color online) Hysteresis loops measured along the principal symmetry directions of the hexagonal lattice for the (a) cp and (b) ucp arrays (ϕ is the angle between the magnetic field and the direction perpendicular to the nanodisks rows, as illustrated in Fig. 2).

small (~ 10 – 20 Oe) in square lattices of Permalloy nanodisks⁶⁴ with approximately the same thickness ($h = 25$ nm) as in our system but with much larger diameter ($D = 700$ nm) and edge-to-edge disk separation ($\Delta l = 100$ nm) than in our case. On one hand, one expects a more pronounced angular anisotropy in a square lattice compared to a hexagonal one, but the much larger disk separation used in Ref. 64 resulted in a weaker magnetodipolar interaction between the nanodisks. For a square lattice of Co nanodisks with $D = 250$ nm, the same thickness as ours ($h = 20$ nm) and the interdisk separation $\Delta l = 50$ nm, a significant anisotropy of the vortex nucleation field (~ 50 Oe) was observed.⁶⁵ This larger effect can be attributed both to another lattice type (square vs. hexagonal) and to a larger magnetization of Co particles (1400 G for Co vs. ≈ 700 G for our Py samples) studied in Ref. 65.

To obtain quasistatic M - H loops from such simulations, we have to find the state with the minimal energy for the given external field sequence, starting each time from the equilibrium state found for the previous field. Rigorous numerical simulations of the transition from the quasiuniform state with $M/M_S \approx +1$ to the vortex state are hardly possible, since this transition corresponds to a spontaneous symmetry breaking of the quasaturated state. Hence, the transition field strongly depends on the details of the nanodisk edge roughness, which is largely unknown. On the contrary, the second transition from the vortex to the quasaturated state with $M/M_S \approx -1$ is fully deterministic. Thus, the satisfactory numerical reproduction of the critical fields obtained experimentally for this last transition can serve as an indicator that all system parameters have been chosen properly.

Taking into account that the system geometry and magnetic material parameters are known from independent measurements, the only degree of freedom left for the fitting of simulated results to experimental data is the magnetization decrease towards the disk edges (inevitably arising during the patterning). Analysis of various types of nonideal edges

carried out for a straight film edge has shown⁶⁶ that the edge tilt and dilution of the edge magnetization both lead to qualitatively the same behavior of the internal field, which plays the main role in the magnetization reversal. In our simulations, we have assumed that the magnetization decreases exponentially toward the disk edges, i.e., it changes as $m(r) = 1 - \exp\{(r - R_c)/r_d\}$, r being the distance to the disk center and R_c the disk radius. The fitting parameter r_d describes the characteristic width of the area near the disk edges, where the magnetization is substantially decreased during the array preparation. The vortex expulsion is governed by the demagnetizing field within the disk, which strongly depends on the magnetization profile near the edges. Hence, the simulated vortex expulsion field should be sensitive to the value of r_d .

Simulation results (solid lines) are presented in Fig. 4 for both the cp and ucp arrays, together with the MOKE loops (open circles). Indeed, the simulated vortex-expulsion field substantially depends on r_d , and a good agreement between measured and simulated data is achieved for a reasonably small value of $r_d = 5$ nm. We also point out that the hysteresis slope in negative fields is also nearly perfectly reproduced in simulations, so that the quasistatic magnetization reversal of our samples can be considered as being fully understood. We also note that the simulated hysteretic behavior did not change noticeably when varying the surface anisotropy in the range $K_S = 0 - 0.6$ erg/cm². This finding shall be important in the analysis of the results of dynamical simulations.

B. Magnetization dynamics: Experimental results

Spin-wave frequencies as a function of the in-plane direction of the applied field are shown in Fig. 5, where ϕ denotes the angle between the field direction and the direction perpendicular to the nanodisks rows (Fig. 2). For both cp and ucp arrays, the magnitude of the applied field is $H = 400$ Oe. The gray-scale plots are the AESWS spectra, while the

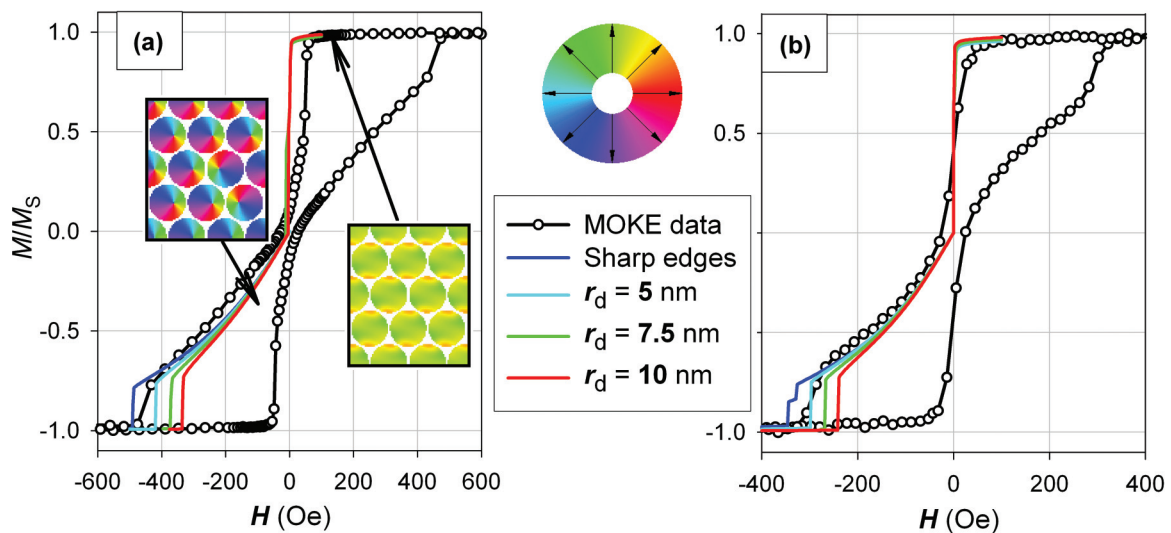


FIG. 4. (Color online) Simulated and measured hysteresis loops for the (a) cp and (b) ucp nanodisk arrays in the field applied in $[0, -1, 1]$ direction (perpendicular to the disk rows, $\phi = 0$). For simulated loops, only the upper hysteresis branch is shown. In negative external fields, simulations have been started from the vortex magnetization state. The insets in (a) show magnetization color maps for a typical quasiuniform magnetization state and a vortex state with the color coding of the magnetization directions presented on the color wheel.

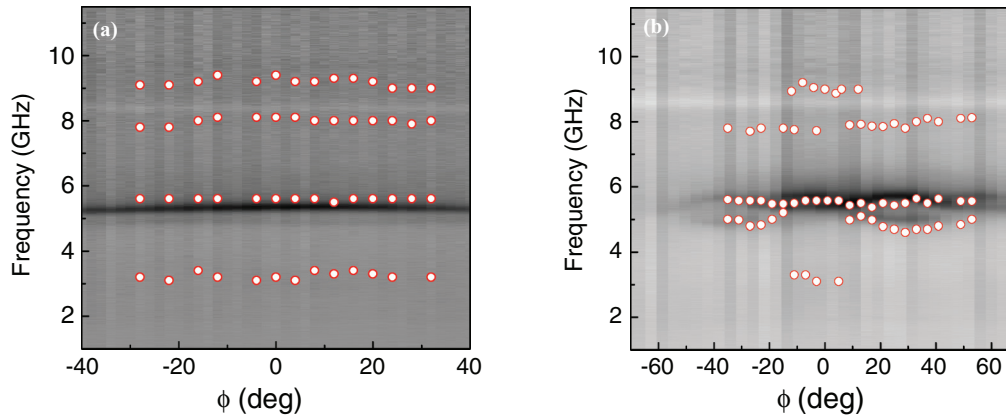


FIG. 5. (Color online) AESWS spectra (gray-scale plots, darker contrast corresponds to higher signal intensity) and BLS frequency data (red circles) as functions of the applied field angle ϕ for the (a) *cp* and (b) *ucp* disks. The in-plane applied field is $H = 400$ Oe. (a) Sample has been saturated at 1000 Oe before measuring the spectra. (b) Field is larger than the saturation field determined by MOKE.

circles represent the BLS frequencies. A very good agreement between AESWS and BLS results for modes detected by the two methods can be seen. We note that BLS was found to detect more spin-wave modes. For the *cp* array, four peaks are detected by BLS in the whole angular range explored, and the frequencies of these modes exhibit an in-plane isotropic behavior [Fig. 5(a)]. On the contrary, for the *ucp* array [Fig. 5(b)], we observe that in addition to the spin-wave mode with the frequency of ≈ 5.5 GHz, which is approximately the same for all angles, we find that close to $\phi = 0^\circ$ another mode appears whose frequency is strongly angle-dependent with a minimum value of ≈ 4.5 GHz close to $\phi = 30^\circ$. The mode at about 7.5 GHz remains almost constant in frequency. The data in Fig. 5 indicates that the magnetodipolar coupling is negligible for the *cp* array, whereas it is appreciable for the *ucp* disks due to the very small edge-to-edge separation in the latter case. A qualitatively similar effect—angular anisotropy of the resonant FMR field H_r —was observed in Ref. 67 for a square lattice of Py nanodisks with the diameter $D = 1 \mu\text{m}$ and thickness $h = 50$ nm for the oscillation frequency corresponding to $H_r \approx 1$ kOe. The effect was explained by nonuniformity of a nanodisk magnetization present even in such relatively high external field. Our theoretical analysis of the angular anisotropy of the AESWS and BLS spectra is presented below in Sec. III C 1 and III C 2.

Evolution of the spin-wave frequencies for the *cp* array as a function of the field magnitude H for the field applied in the $[2, -1, -1]$ direction (i.e., \mathbf{H} parallel to the dot rows) is shown in Fig. 6. Coming from positive saturation and decreasing the field value, we observe that the frequencies of one prominent (fundamental) mode and several weaker branches monotonously decrease. Close to $H = 0$, the field dependencies change abruptly. Decreasing H further, the most prominent branch observed in the AESWS data reappears at $H = -400$ Oe and follows a field dependence for $H < -400$ Oe, which is mirrored with respect to $H > 400$ Oe. Frequencies measured in the vortex configuration for $-400 \text{ Oe} < H < 10$ Oe are not shown because the analysis of this state is out of the scope of this work.

The field dependencies of the spin-wave frequencies for the *ucp* sample are shown in Fig. 7 for the field \mathbf{H} applied in the

$[0, -1, 1]$ direction (i.e., \mathbf{H} perpendicular to the dot rows) and $\phi = 30^\circ$ (\mathbf{H} parallel to the dot rows). Similar to the previous case, for both field orientations it can be seen that, starting from the positive saturation, we observe the transition from the quasisaturated state to the vortex one at $H \approx 0$ and the vortex expulsion at $H \approx -300$ Oe, in good agreement with the hysteresis loops.

C. Magnetization dynamics: Theoretical results

First, we present in Fig. 8 two examples for the field dependencies of the oscillation power spectra for the m_y -magnetization component (in-plane component perpendicular to the bias field \mathbf{H}). Figure 8(a) displays spectra obtained for a spatially homogeneous excitation. As explained above, in a patterned array a spatially homogenous pulse may excite modes with nodal lines perpendicular to \mathbf{H} (BA-like

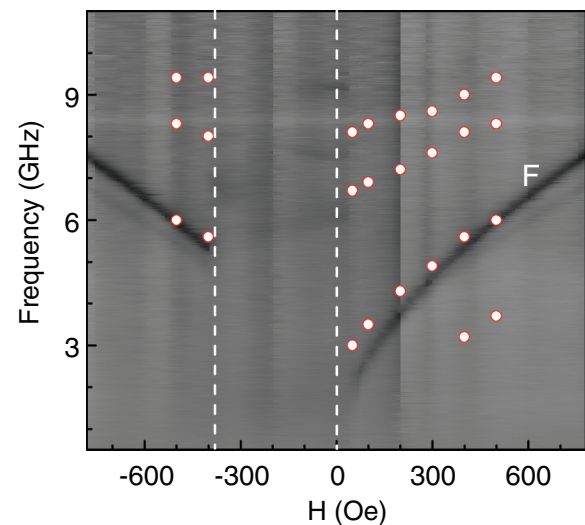


FIG. 6. (Color online) AESWS spectra (gray-scale plots) and BLS data (red circles) as functions of the magnitude of the external field applied in the $[2, -1, -1]$ direction (i.e., parallel to the disk rows) for the *cp* array. The magnetic field was swept from positive to negative saturation. The vertical dashed lines mark the vortex-state field range.

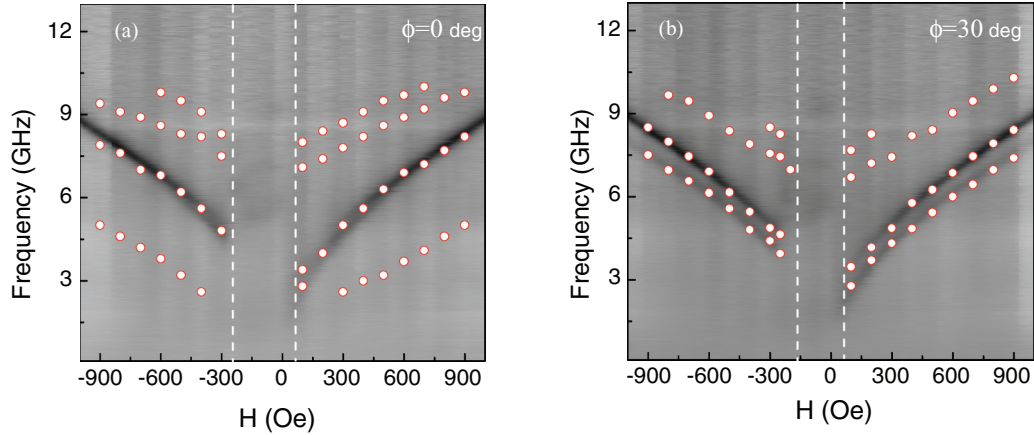


FIG. 7. (Color online) AESWS spectra (gray-scale plots) and BLS data (red circles) for the *ucp* nanodisk array as functions of the magnitude of the magnetic field applied (a) in the $[0, -1, 1]$ direction (perpendicular to the dot rows) and (b) in the $[2, -1, -1]$ direction (parallel to the dot rows).

modes), visible both in AEWS and BLS spectra. A spatially nonhomogeneous field pulse with one or more nodal lines parallel to \mathbf{H} (see Sec. II C) may excite modes with nodal lines also parallel to \mathbf{H} (DE-like modes).

Verification of system parameters. We have started with simulations of the *cp* array because experimental data presented above indicate that in this sample the interaction between nanodisks is negligible. This way we could verify that material parameters used in quasistatic simulations are also suitable to reproduce the dynamical behavior of our samples.

Comparison of the field dependences of the fundamental mode frequency obtained in simulations and in FMR experiments is presented in Fig. 9. As clearly seen, simulated and measured values agree well only if we assume that the surface anisotropy is zero in the disk array ($K_s = 0$). This discrepancy between the values of K_s obtained for the continuous film and the disk array can be due to the altering of the surface structure (and hence the surface anisotropy) of the disks during the array patterning process. Based on this result, we have

assumed in all further simulations that the surface anisotropy is absent.

1. Dynamics of the *ucp* array for the bias field \mathbf{H} applied in the $[0, -1, 1]$ direction (perpendicular to the nanodisk rows)

In this subsection, we analyze the results obtained by DMM and micromagnetic simulations for the *ucp* sample, with the field \mathbf{H} in the $[0, -1, 1]$ direction. Due to the hexagonal arrangement of nanodisks for this particular orientation of \mathbf{H} , magnetic poles formed at the edges of each disk are relatively far from analogous poles on the nearest-neighbor disks. For this reason, an *S* state^{68,69} is formed as the equilibrium configuration of nanodisks [Fig. 10(a)]. The formation of the *S* state is also favored by a small misalignment of \mathbf{H} with respect to the lattice symmetry axis (used in simulations to avoid artificial degeneracy and unavoidable in a real experiment), but we shall see below—by simulating the system with \mathbf{H} parallel to the disk rows—that this misalignment alone is not sufficient to produce the *S* state.

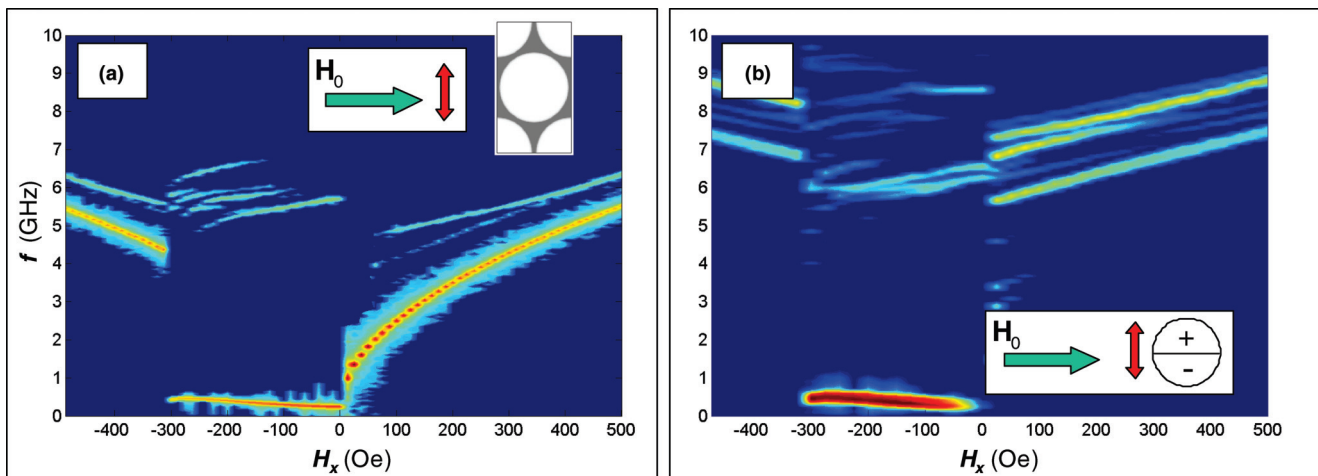


FIG. 8. (Color online) Example of simulated spectra excited by the (a) spatially homogeneous and (b) nonhomogeneous excitation pulses. Direction of the bias field \mathbf{H} is shown with the green arrow; the excitation pulse is directed perpendicular to the array plane. Spectra in the field region $-300 \text{ Oe} < H_x < 0$ correspond to the vortex dynamics [see Fig. 4(b) for the field region where vortices do exist] and shall be discussed in more detail elsewhere.

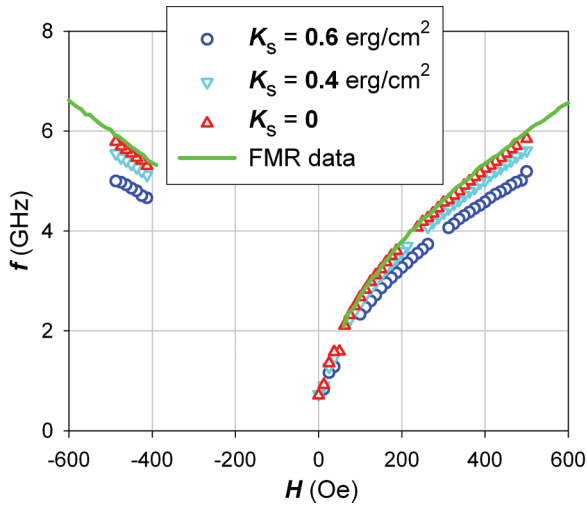


FIG. 9. (Color online) Comparison of simulated (symbols) and measured by AESWS (solid green line) frequencies of the fundamental mode in the cp array is shown; results only for the quasiuniform magnetization states are shown. Simulations agree with the experimental data for $K_s = 0$ erg/cm².

Magnetization configurations with strong uncompensated magnetic surface charges are usually quite sensitive to the changes of the external field when this field is below the saturating field. Since the mode profiles should depend on the equilibrium magnetization state, we expect that these profiles will undergo significant changes as the magnetic field is varied.^{70,71} For the field \mathbf{H} parallel to the disk rows, when magnetic charges of opposite signs are formed at the adjacent edges of the neighboring disks, these charges largely compensate each other, and the situation is different, as will be shown in Sec. III C 2.

To proceed with our analysis, we note first that in DMM calculations either magnetic or nonmagnetic discretization cells are considered, so the magnitude of the reduced-cell magnetization $m_i(\mathbf{r}) = M_i(\mathbf{r})/M_S$ is either 1 or 0, respectively; we shall call a shape made of such cells a binary shape. In the

following subsection, we present calculations performed in this binary-shape model, both in DMM and MicroMagus, in order to compare the results. Then, in Sec. III C 1 b, we present calculation results obtained by micromagnetic simulations performed with the MicroMagus package using the smooth shape ($0 \leq m_i(\mathbf{r}) \leq 1$). Comparing the latter results to the case of the binary shape, we show that a gradual decay of the magnetization magnitude toward the disk edges is necessary to obtain a satisfactory agreement to experimental data.

(a) *Numerical results for the binary shape: Comparison of simulation methods.* We present this comparison in Figs. 10 and 11, displaying only results for BA-like modes, in order not to overload the graph. First, we note that for those fields, where eigenmodes are found both by DMM and micromagnetic simulations, eigenfrequencies (Fig. 10) and spatial distributions of the oscillating power obtained by both methods agree very well.

From micromagnetic simulation results, we show only modes with sufficiently large amplitude (with the spectral power larger than 10^{-4} of the maximal power of the fundamental mode). Mode amplitudes can significantly vary in the field interval under study. In particular, modes C and D in Fig. 10 could be seen in micromagnetic simulations spectra only in fields larger than $H_{\min}(C) \approx 320$ Oe and $H_{\min}(D) \approx 150$ Oe. This feature can be explained by the varying strength of coupling between the modes and the excitation used in micromagnetic simulations, and the redistribution of energy between the modes after the excitation pulse has been switched off. The same qualitative behavior is observed in real AESWS experiment, where higher modes are visible only starting from some minimal bias field. Results of DMM, instead, provide the full spectrum of eigenmodes, independently of their excitation amplitude in real experiments.

To classify the modes, we have to resort to their spatial maps, which are displayed in Fig. 11 for several values of the bias field. For each mode, we show both a linear map of its amplitude (left map in each pair of maps) and a log-scale map of its oscillation power (right map in each pair). The log-scale power maps are helpful for the mode classification,

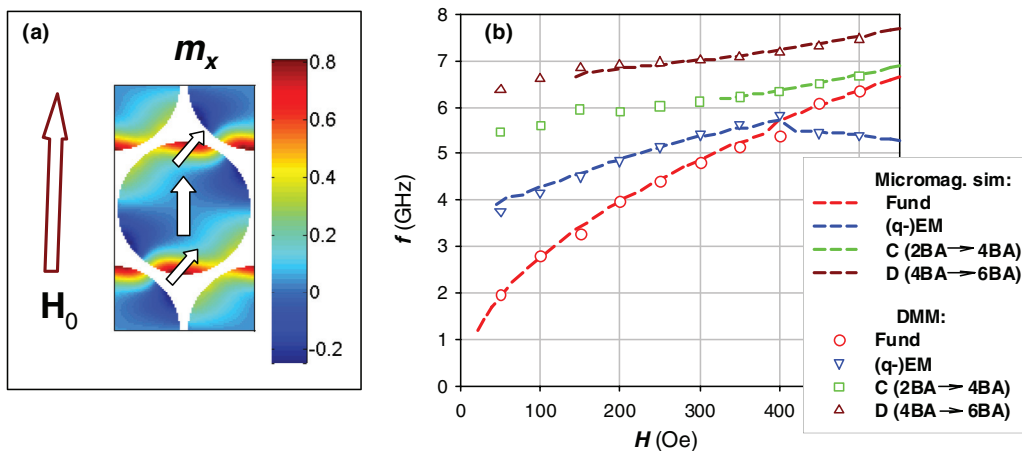


FIG. 10. (Color online) (a) Equilibrium magnetization state as a color map of the m_x projection for \mathbf{H} in the $[0, -1, 1]$ direction (perpendicular to disk rows). (b) Mode frequencies for the ucp array obtained via DMM (open circles) and full-scale micromagnetic simulations (dashed lines). In micromagnetic simulations, the exciting field was spatially homogeneous. A perfect agreement between the methods can be seen in all cases where an eigenmode was found by both methods.

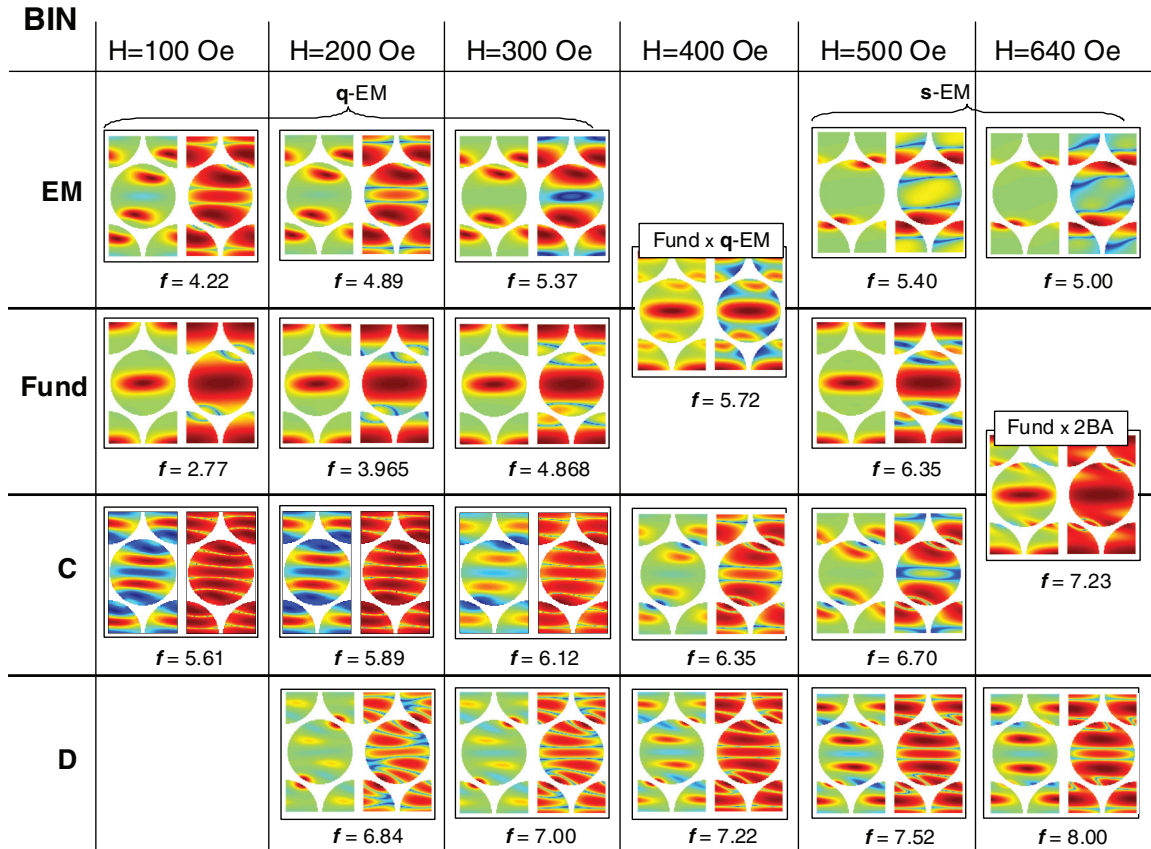


FIG. 11. (Color online) Evolution of eigenmodes whose $f(H)$ dependencies are presented in Fig. 10, with decreasing bias field (\mathbf{H} in the $[0, -1, 1]$ direction, i.e., perpendicular to nanodisk rows). Here and on subsequent figures, mode maps are taken from micromagnetic simulations. In each map pair, on the left the spatial map of the spectral amplitude of oscillations (with sign) using linear scale (here blue indicates negative amplitudes; red indicates positive amplitudes) is shown; on the right, maps of the oscillation power on the log-scale (blue indicates small power; red indicates large power) is shown. Note how the number and location of the nodal lines changes with the decreasing bias field, especially for modes C and D.

revealing the presence of the nodal lines much better. A detailed discussion of the different modes is presented below.

Fundamental mode. From Fig. 11 it is clear that the mode marked with the red dashed line and red circles in Fig. 10 is the fundamental mode (denoted as Fund): Its amplitude does not change sign across the nanodisk, and the overwhelming majority of its power is concentrated in the central region of the disk. Small amplitude maxima visible at the disk edges only on the log-scale maps are due to the strong demagnetizing field near these edges and do not have any noticeable effect on the mode character. The only significant change in the power distribution is observed when the $f(H)$ curve for this mode crosses those of other modes, namely the edge mode (EM) (at $H \approx 400$ Oe) and of the C mode (at $H \approx 640$ Oe). An important point is that the power distribution of the fundamental mode is strongly inhomogeneous even for the highest studied fields, demonstrating once more a large influence of edge effects in nanopatterned structures. Finally, the sublinear behavior of the frequency below 100 Oe is due to the increasing instability of the S state, which leads to the softening of the fundamental mode as the bias field is reduced. This means that at some critical field magnetic moments in the inner-nanodisk region, where the oscillation amplitude of the fundamental mode is

the largest, will be involved first in the transition to the vortex state.⁷¹

Edge modes. The lowest frequency mode observed at high fields ($H > 400$ Oe) is the EM: its oscillation power is concentrated primarily near the disk edges perpendicular to the field direction, as can be seen on the linear scale maps of this mode for $H = 500$ Oe and 640 Oe (Fig. 11). The strong localization of this mode is due to the demagnetizing field near the corresponding nanodisk edges, which is especially strongly localized for a binary shape. A detailed description of an analogous localization effect for rectangular nanoplatelets can be found in Refs. 46 and 72. An even more complex localization of EMs in vortex-containing and saturated ring-shaped elements can be found in Ref. 73 (see also Ref. 74 for the discussion of the difference of $f(H)$ slopes between the EMs and volume modes). The spatial distribution of this mode changes significantly due to hybridization effects when its $f(H)$ dependence crosses the corresponding curve of the fundamental mode at $H_{F=EM} \approx 400$ Oe. Below this field, the maximal oscillation power of the EM is achieved not at the disk edge but in the region close to this edge inside the nanodisk. Also, the oscillation amplitude of this mode in the central region increases but still remains at least one order of

magnitude smaller than the value near the disk edge. For this reason, and also to keep the same mode notation along the whole $f(H)$ curve, we propose to label this mode for fields $H < H_{F=EM}$ as the quasi-EM (q-EM). Very similar behavior as a function of the bias magnetic field was observed by Keatley *et al.*¹⁹ for arrays of square magnetic nanoelements

Another interesting feature of this mode is the strongly nonmonotonous field dependence of its frequency. For high fields ($H > 1$ kOe, not shown in the figures), the EM frequency shows a linear field dependence, because the demagnetizing field \mathbf{H}_{dem} remains nearly constant. As the field decreases, the magnetization at the disk edges starts to align along the edges (in order to decrease the self-demagnetizing energy), deviating from the field direction. This leads, in turn, to the decrease of the demagnetizing field magnitude; this decrease is faster than the decrease of the bias field. Taking into account that the demagnetizing field is directed opposite to the bias field, the total field $\mathbf{H}_{tot} = \mathbf{H} + \mathbf{H}_{dem}$ near the disk edges increases. This total field increase results in the increase of the mode frequency. Finally, when the external field is so small that magnetic moments near the edges are nearly aligned along the edges, \mathbf{H}_{dem} changes very weakly compared to the decrease of the external field. In these external fields the mode frequency decreases again when H continues to decrease.

Higher BA modes. The classification of higher modes is more complicated due to the nontrivial behavior of their nodal lines when the bias field is decreased. For example, for the C mode in Figs. 10 and 11, two nodal lines in the bulk of the nanodisk are clearly seen at all fields. However, two additional nodal lines exist, which for high fields ($H > 450$ Oe) are very short and positioned close to the disk edges (see the log-scale map for the mode C in Fig. 11 for $H = 500$ Oe). Hence, these short lines can be considered as the consequence of the strong demagnetizing field near these edges, and thus they could be neglected by the mode classification. In this case,

according to the general classification rules,⁷⁵ in high fields this mode should be called the 2BA mode. However, when the field decreases below ≈ 400 Oe, the two edge nodal lines start to move toward the nanodisk center so that already at $H = 300$ Oe they are definitely the fully developed bulk nodal lines, converting the mode into the 4BA. For this reason, we denote this mode as C (2BA \rightarrow 4BA). The situation is even more complicated for the next higher mode (see the last row in Fig. 11), where not only the position but also the number and connectivity of nodal lines change by decreasing H . The nodal line near the edge has the L form at $H = 640$ Oe and evolves gradually into two nodal lines when the field is decreased to 200 Oe. We denote this mode as D (4BA \rightarrow 6BA).

(b) *Comparison of simulation results for the binary shape and smoothed edges: BA-like modes.* Next, we compare the system of nanodisks discretized by the binary shape and a system with magnetization decreasing toward the disk edges, as described in Sec. III A. We have also employed the feature of the MicroMagus package, which allows us to reduce the cell magnetization according to the fraction of the cell contained inside a curved element boundary. We denote the shape obtained after the last two operations as a smoothed-edge shape. Comparison of the mode frequencies as functions of the bias field for these two shapes is given in Fig. 12, and spatial mode maps for nanodisks with smoothed edges are displayed in Fig. 13.

Fundamental mode. The influence of different discretization of the disk edges on the fundamental mode is relatively small because this mode is localized in the central disk region. The only significant difference (due to the mode hybridization) is seen for fields where the $f(H)$ dependence for the F mode intersects $f(H)$ branches for other modes.

Edge modes. The main difference between the two systems (binary and smoothed shapes) is the striking change in the frequency of the EM—compare solid and dashed blue lines

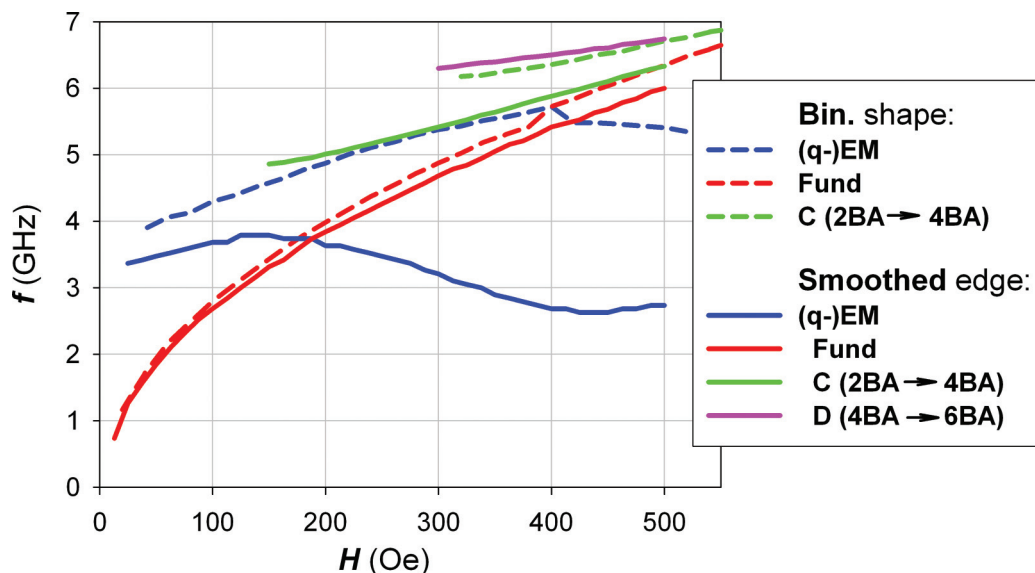


FIG. 12. (Color online) Comparison of eigenmode frequencies (obtained by micromagnetic simulations) of the *ucp* array discretized using the binary shape (dashed lines) and the nanodisks with smoothed edges (solid lines), for \mathbf{H} in the $[0, -1, 1]$ direction (perpendicular to disk rows). Dramatic change in the behavior of the EM and substantial frequency shift of other modes—except of the fundamental one—can be seen.

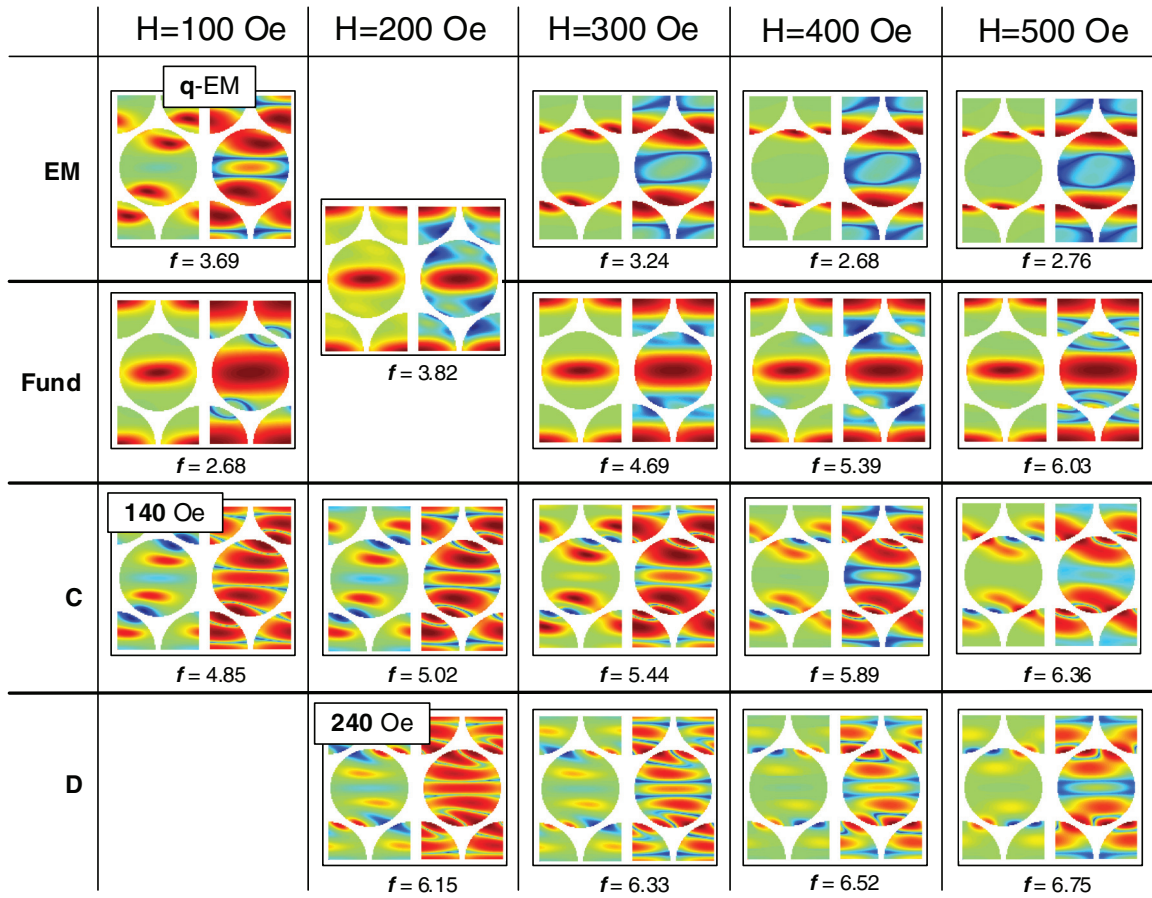


FIG. 13. (Color online) The mode evolution with the bias field (\mathbf{H} in the $[0, -1, 1]$ direction, or perpendicular to disk rows) presented in the same manner as in Fig. 11 but for the smoothed edges shape.

in Fig. 12. This is a direct consequence of a very different treatment of the nanodisk edges for smoothed and binary shapes. When changing to the smoothed shape, two effects occur. First, the maximal value of the demagnetizing field \mathbf{H}_{dem} created by the disk edges decreases so that the EM frequency should increase (because \mathbf{H}_{dem} is directed opposite to the bias field). However, on the other hand, the area where this demagnetizing field is localized is considerably wider for the smoothed shape than for the binary one. For this reason, the EM for the smoothed shape is localized less strongly than for the binary one, which is the result in the decrease of its frequency. The latter effect is stronger than the frequency increase caused by the smaller H_{dem} , so that the net result is the much lower frequency of the EM for the smoothed shape. A qualitatively similar effect—the decrease of the EM frequency when the edge is nonideal—was observed in simulations⁶⁶ for the case of a straight edge of a thin film when the in-plane external field is perpendicular to the edge.

Higher BA modes. Evolution of the power distribution for higher modes C and D with decreasing the bias field is shown in Fig. 13. Using the same arguments as for the binary shape, we denote the mode C as 2BA \rightarrow 4BA and mode D as 4BA \rightarrow 6BA. Mode C was observed down to $H = 140$ Oe, and mode D was observed up to $H = 240$ Oe, as marked in Fig. 13.

The most interesting feature of mode C is that below $H = 400$ Oe its frequency (for the smoothed shape) nearly coincides

with the frequency of the q-EM mode for the binary shape. Another nontrivial finding is that frequencies of the D mode for the smoothed shape and of the C mode for the binary shape are very close in the whole interval of fields where both these modes are visible. The most likely explanation for this nontrivial phenomena could be a similar localization of the oscillation power of corresponding mode pairs inside the nanodisk, i.e., far from the disk edges. To prove this idea, we have plotted the amplitudes of these mode pairs for the same field in Fig. 14. Oscillation amplitudes near the disk edges are very different due to different edge discretizations, so that normalization to the maximal amplitude used in Fig. 13 would hide the similarity we are looking for. For this reason, in Fig. 14 we have normalized the oscillation amplitude to the maximal amplitude of the bulk peaks (see the double-side arrows). From the maps in Fig. 14 it is evident that the width and shapes of the bulk peaks for the binary q-EM-mode and smoothed C mode are nearly identical. For the binary C mode and smoothed D mode, these bulk peaks are very similar. Taking into account that the mode frequency is determined by its localization pattern (which, in turn, defines the spatial Fourier spectrum of the mode responsible for the mode frequency), this similarity of the bulk peaks provides the explanation for the close $f(H)$ dependencies of these spectral branches.

(c) *Comparison of simulation results for the binary shape and smoothed edges: DE-like modes.* For the modes excited

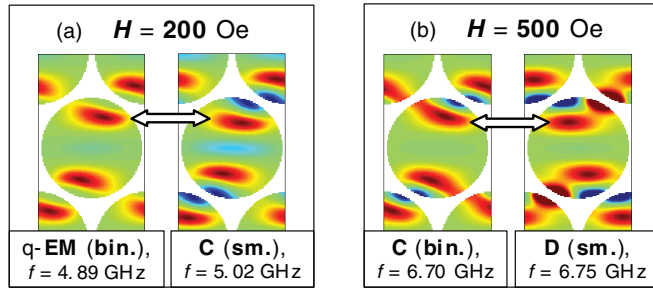


FIG. 14. (Color online) Amplitudes of the following pairs: (a) q-EM-mode for the binary shape and C mode for the smoothed shape; (b) C mode for the binary shape and D mode for the smoothed shape. Double-sided arrows indicate the bulk oscillation peaks, whose shapes and locations are very similar for each specific pair, thus leading to the close-mode frequencies.

by an external field that is nonhomogeneous on the nanodisk length scale or by nonhomogeneous thermal fluctuations, one or more nodal lines along the bias field \mathbf{H}_{ext} are always present. This means that the mode amplitude near those edges of a nanodisk, which are perpendicular to \mathbf{H}_{ext} , is usually quite small. Hence, the strong demagnetizing field induced by these edges does not play such a significant role for this mode type as for AESWS-active modes. For this reason, we can expect that results of micromagnetic simulations employing the smoothed edges and DMM results for the binary form should agree reasonably well.

This expectation is confirmed by Figs. 15 and 16, where $f(H)$ dependencies for the DE modes (Fig. 15) and the evolution of their profiles with external field (Fig. 16) are shown. It can be seen that for 1DE and $2BA \times 1DE$ modes, where the oscillation power is very small near the edges where the \mathbf{H}_{dem} is high (first and last map rows in Fig. 16), mode frequencies obtained by micromagnetic simulations and DMM coincide very well. For the $xBA \times 1DE$ mode (middle row in Fig. 16) the coincidence is worse, especially for higher fields, where the oscillation power in these edge regions is higher (we call this mode $xBA \times 1DE$, because

the complicate configuration of node lines perpendicular to \mathbf{H}_{ext} does not allow the unambiguous mode identification). Finally, the $2BA \times 2DE$ mode obtained in DMM is not visible in micromagnetic simulations due to its specific symmetry, which is incompatible with the symmetry of excitation field used in simulations.

2. Dynamics of the ucp array for the bias field \mathbf{H} applied in the $[2, -1, -1]$ direction (parallel to the nanodisc rows)

As shown above, for the binary shape, results of micromagnetic simulations and DMM fully agree. For this reason we do not repeat this test for the bias field \mathbf{H} oriented parallel to the nanodisk rows; rather we begin the analysis of this case comparing results of micromagnetic simulations performed on disks with smoothed edges with DMM calculations performed for the binary shape.

(a) *Binary shape vs. the shape with smoothed edges: BA modes.* Results of this comparison for modes excited by the homogenous ac-field are shown in Fig. 17. First, we point out that the EM is now absent because the distance between the nanodisk edges in the direction parallel to the dot rows is very small. For the *ucp* array, the edge-to-edge disk separation is approximately the same as the nanodisk thickness (20 nm). For this reason, the self-demagnetizing field near the corresponding nanodisk edges is largely compensated by the stray field from its nearest neighbors so that the mode localized near these edges does not exist.

Frequencies of the fundamental mode obtained for the smoothed and binary shapes agree very well at high bias fields (above 250 Oe), while the agreement becomes increasingly worse when the bias field decreases. This behavior can be explained by the larger influence of the edge shape for smaller bias fields: the smaller the bias field, the more important the detailed configuration of the demagnetizing field coming from the nanodisk edges, so that the magnetization state depends on the exact element shape more strongly.

Another interesting observation is the qualitative difference of the fundamental mode profile for the bias field \mathbf{H}_0 directed parallel (upper maps on the right of Fig. 17) and perpendicular (second row of images in Fig. 11) to the disk rows. The most

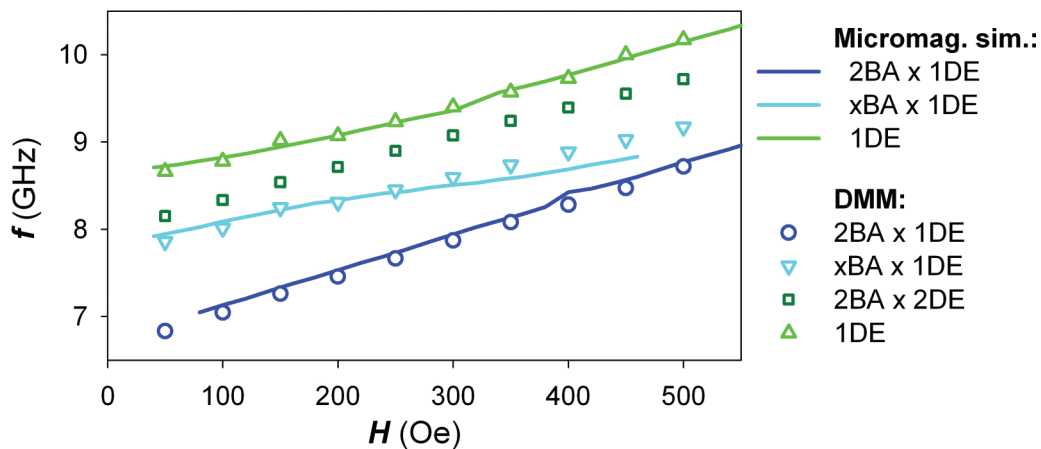


FIG. 15. (Color online) Comparison between frequencies of the DE-like modes for the *ucp* array in the bias field \mathbf{H} in the $[0, -1, 1]$ direction (perpendicular to the nanodisk rows) obtained by micromagnetic simulations for the smoothed shape and by DMM employing the binary shape. A good agreement between both methods for most cases can be seen.

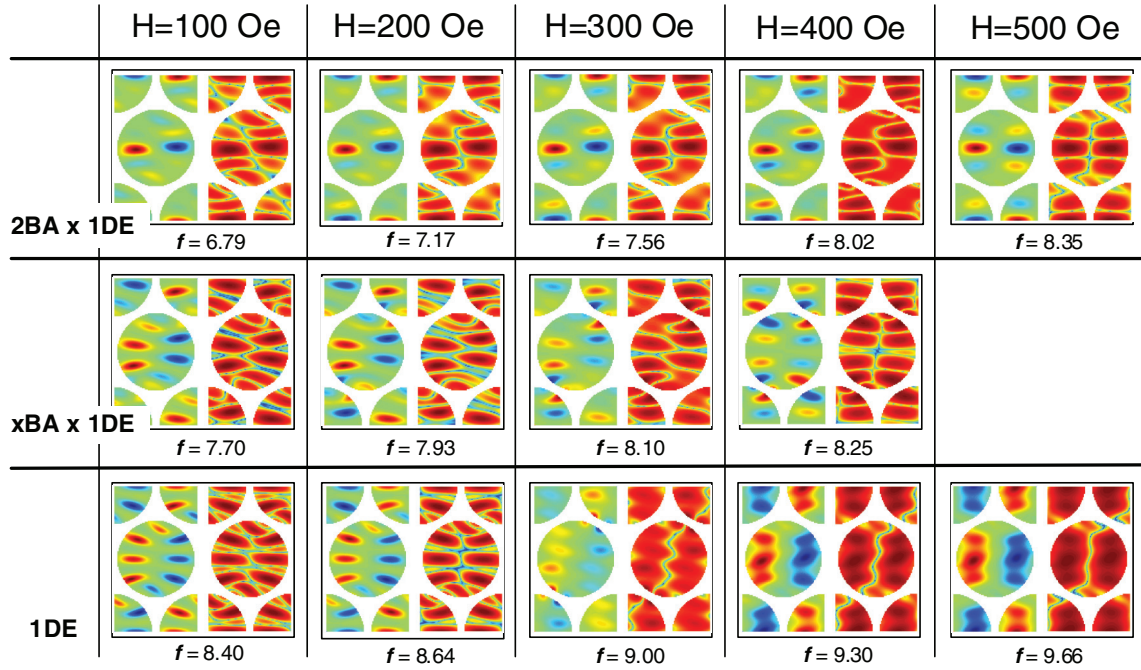


FIG. 16. (Color online) Spatial profiles of the DE-modes, where $f(H)$ dependence is shown in Fig. 15 (\mathbf{H} in the $[0, -1, 1]$ direction, i.e., perpendicular to disk rows). As a general trend, it can be seen that with decreasing field, the vertical nodal line (along the bias field) becomes more complicate, and the spatial mode structure—especially for the 1DE mode—becomes more inhomogeneous.

probable explanation is the following. First, regions with the high oscillation power form the stripes that are perpendicular to \mathbf{H}_0 (as usual for BA modes). Second, these stripes are positioned within the nanodisks so that the edge-to-edge separation between these stripes in neighboring nanodisks is minimal (this way the total stray field near the edges is minimized and the energy required for the mode excitation decreases).

For higher modes, we observe a good agreement between the frequencies obtained by DMM (binary shape) and micromagnetic simulations (smoothed shape). For micromagnetic

simulations, we determine that in the field interval $H \approx 250\text{--}400$ Oe, the 2BA and 4BA modes (see corresponding maps in Fig. 17, right panel) are very close in frequency and have an appreciable power. For smaller fields (from $H \approx 100$ to 250 Oe) only the 2BA mode is visible. Above 300 Oe, the frequencies of 2BA and 4BA modes tend to converge: until above $H \approx 400$ Oe, only a single peak is observed. In DMM calculations, the 2BA and 4BA converge in frequency only at higher fields (above 500 Oe). The reason why the power of the 4BA mode becomes almost equal to that of 2BA is that with increasing the bias field the 4BA mode tends to damp

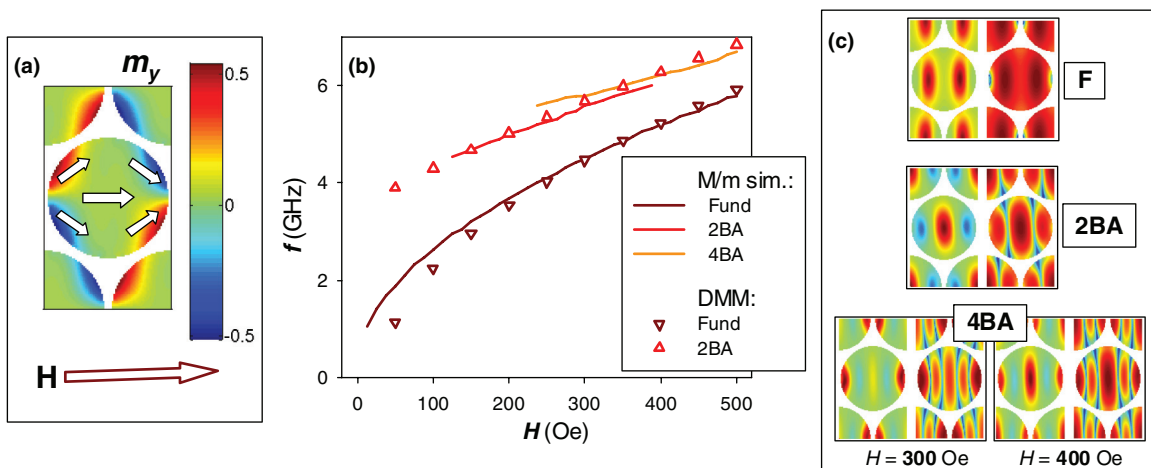


FIG. 17. (Color online) (a) Equilibrium magnetization state as the m_y color map for \mathbf{H} in the $[2, -1, -1]$ direction (parallel to the disk rows). (b) $f(H)$ dependencies for BA modes obtained by micromagnetic simulations (solid lines) and DMM (open circles). (c) Spatial mode maps (from micromagnetic simulations). Note a significant change in the power distribution for the 4BA mode when the field is increased from 300 Oe to 400 Oe, so that the 2BA mode is no longer observed.

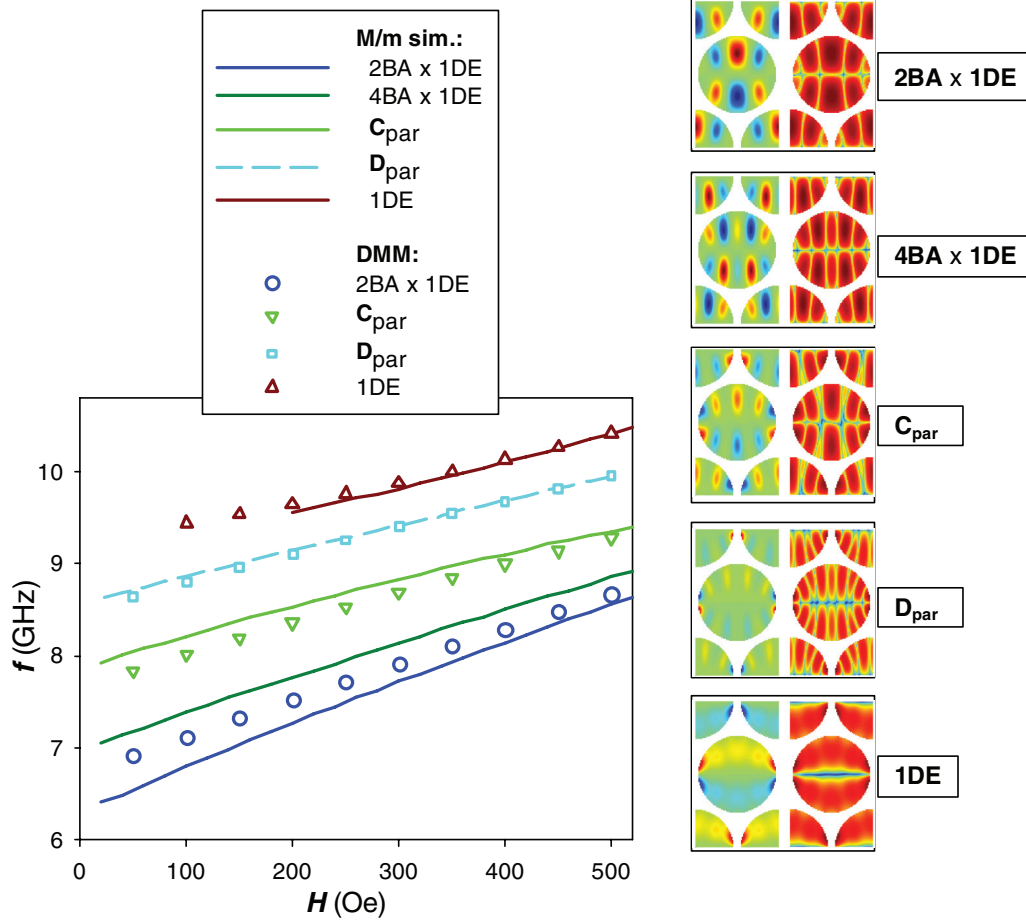


FIG. 18. (Color online) The same as in Fig. 17 for DE-like modes. Mode maps are given for $H = 300$ Oe.

oscillations in the bulk and becomes similar to a symmetric EM.

(b) *Binary shape vs. the shape with smoothed edges: DE modes.* For \mathbf{H}_0 parallel to the nanodisk rows, magnetic poles of neighboring disks in the equilibrium state are located very close to each other. Hence, the total demagnetizing field near the nanodisk edges is significantly smaller than for the case of \mathbf{H}_0 perpendicular to the nanodot rows and the equilibrium leaf state [Fig. 17(a)] changes insignificantly by variation of the applied field. Thus, only minor modifications of the mode profiles are found in the bias field interval studied here. For this reason, in Fig. 18 we present these profiles only for $H_0 = 300$ Oe (profiles obtained by micromagnetic simulations and DMM are essentially the same).

Figure 18 shows the spin-wave frequencies calculated by DMM and micromagnetic simulations performed using a nonhomogeneous pulse. The agreement is worse than for the case where \mathbf{H}_0 is perpendicular to the disk rows (compare Fig. 18 to Fig. 15). In particular, for the $2BA \times 1DE$ and the C_{par} modes the difference between the frequencies for the binary and smoothed shapes have opposite signs: for the $2BA \times 1DE$ mode the frequency is higher for the binary shape, for the C_{par} mode it is higher for the smoothed one. This considerable difference in the frequency between systems where the disk edges are treated differently is due to the

relatively large oscillation power near the disk edges parallel to the x direction (horizontal direction in this figure)—see three upper maps in Fig. 18. The opposite signs of the frequency differences $f_{\text{bin}} - f_{\text{smooth}}$ for these two modes might be due to a qualitatively different behavior of the mode amplitude. Inspection of the amplitude maps in Fig. 18 reveals that in each half of the disk (upper or lower) for the $2BA \times 1DE$ mode, the sign of the magnetization projection oscillates along the horizontal direction, whereas for the C_{par} mode it remains mostly constant (although the value of the amplitude changes very strong), changing near the ends of the horizontal nodal line only. This behavior leads to the opposite signs of the dynamical interdot coupling for the $2BA \times 1DE$ and C_{par} modes and to the corresponding difference in their behavior for the binary and smoothed shapes.

For the modes that we classify as D_{par} (to distinguish it from the D mode shown in Figs. 12 and 13) and 1DE, the agreement between the frequencies obtained for smoothed and binary shape is very good. For these modes, the oscillation power is concentrated mainly near the disk edges parallel to the vertical axis—see maps in Fig. 18. In these regions, the static demagnetizing field is relatively small for the reasons explained above. First, the angle between the magnetization and the tangent to the disk surface is small (so that the static self-demagnetizing field by itself is low); second,

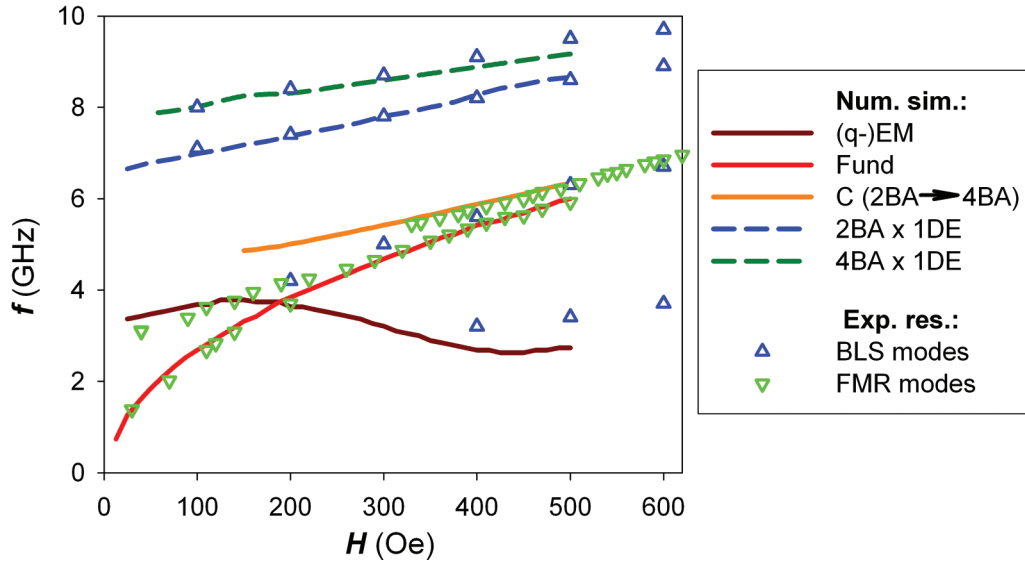


FIG. 19. (Color online) Comparison between numerical results (solid lines for BA-like modes and dashed lines for DE-modes) with experimental data (green triangles down indicates AESWS; blue triangles up indicates BLS) for the *ucp* array in the in-plane external field \mathbf{H} oriented in the $[0, -1, 1]$ direction (perpendicular to the disk rows).

both static and dynamic self-demagnetizing fields are largely compensated by the corresponding dipolar fields from nearest-neighbor disks.

Concluding this part of discussion, we would like to emphasize that dynamic phenomena observed in our study are highly complex. Not only the ground state and the internal magnetic field profiles vary, but the coupling between different elements of the array also vary—all with the applied field. Nonetheless, it might be tempting to apply some kind of analytical or semi-analytical theory (see, e.g., Refs. 40–44) to draw conclusions more general than those presented here based on the micromagnetic simulations (at least at the larger bias field values). However, although such theories have an inherent advantage over simulations by facilitating a simpler generalization, this advantage quickly diminishes as the complexity of the observed phenomena increases. The present case is definitely beyond the complexity level below which the requested sort of generalization could be possible. Moreover, it might prove formidable to achieve a reasonable agreement between simulations and semi-analytical calculations even in the case of a pair of interacting nanoelements in the magnetically saturated state.⁷⁶ A good description of the field dependence of the spin-wave spectrum should be expected to be even more challenging.

D. Magnetization dynamics of the *ucp* array: Comparison between theory and experiment

1. Comparison for the bias field in the $[0, -1, 1]$ direction (perpendicular to the nanodisc rows)

For the constant bias field oriented perpendicular to the nanodisc rows, comparison between frequencies calculated by micromagnetic simulations and data obtained using both AESWS and BLS is shown in Fig. 19. Here we have plotted only those numerically obtained modes that correspond to the experimentally observed ones. The complicated questions

of why some modes have a larger intensity in experimental observations than others, and why some modes are not visible at all, will be discussed elsewhere.

Solid lines in Fig. 19 show frequencies of the modes excited in simulations by the homogeneous field pulse, dashed lines show frequencies excited by the pulse $h_z(\mathbf{r}) = h_0 \sin(2\pi x/L_x) \cdot \cos(2\pi y/L_y)$. Modes excited by pulses with other spatial symmetries were either very weak or have been already observed for the homogeneous excitation or $h_z(\mathbf{r})$ given above.

It can be clearly seen that for this bias field orientation we have a nearly perfect agreement between simulated and measured frequencies, except for the EM at $H > 300$ Oe. The agreement for this mode is not as good as for the other modes, because the magnetization profile near the nanodisk edge plays a decisive role for the EM frequency; this profile is not known exactly. However, we point out that this still reasonably good agreement is obtained using the same magnetization decrease profile near the disk edges as that used to fit the MOKE hysteresis loop. We point out that for the binary shape, the corresponding agreement would be very poor (see the dashed blue line in Fig. 12).

In summary, for this bias field direction, the comparison of theoretical and experimental results enables an unambiguous identification of the mode types observed experimentally. This is very important not only for gaining deeper insights into the fundamental properties of the nanoelement arrays but also for the development of various magnonic applications.

2. Comparison for the bias field in the $[2, -1, -1]$ direction (parallel to the nanodisc rows)

Comparison between simulated and measured frequencies for the bias field \mathbf{H}_0 in the $[2, -1, -1]$ direction (parallel to the nanodisc rows) is presented in Fig. 20. Again, solid lines in this figure show frequencies of the modes obtained for a spatially homogeneous excitation pulse; dashed lines are

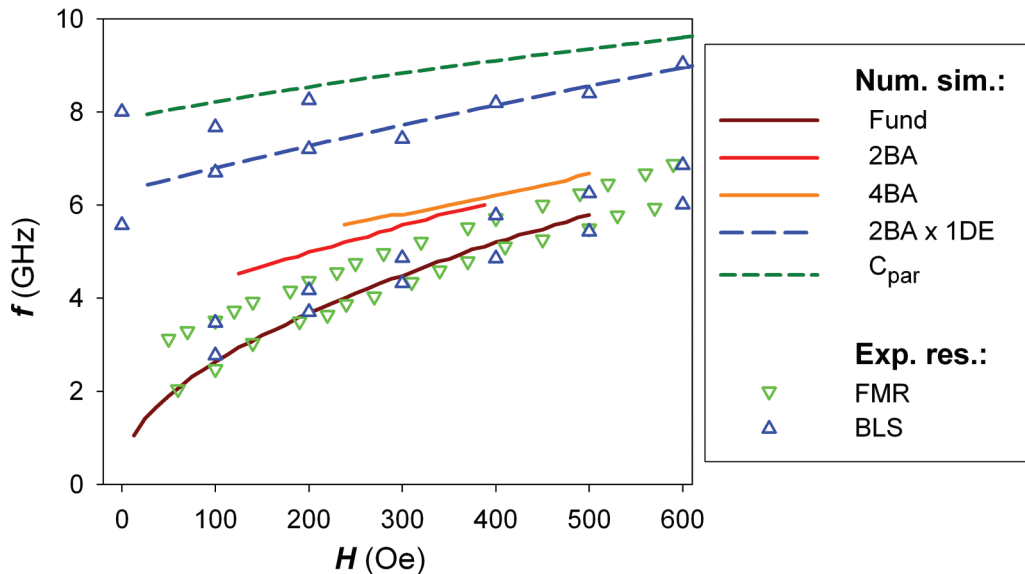


FIG. 20. (Color online) The same as in Fig. 19 for the external bias field \mathbf{H}_{ext} oriented in the $[2, -1, -1]$ direction (parallel to the nanodisk rows).

shown by the field pulse that has the spatial profile $h_z(\mathbf{r}) = h_0 \cdot \cos(2\pi x/L_x) \cdot \sin(2\pi y/L_y)$ for this orientation of \mathbf{H}_0 .

For the two highest modes (visible in BLS only), we have in our disposal two simulated modes, frequencies of which exactly agree with the experimental data: the $2\text{BA} \times 1\text{DE}$ mode and the C_{par} mode (see Fig. 18 for the corresponding power maps). As for the case of the external field applied perpendicular to the nanodisk rows, this agreement enables the unambiguous identification of the modes observed experimentally.

Finally, with reference to Fig. 5 (right panel), we can now say that the modes that give the largest AESWS and BLS signals with the characteristic sixfold symmetry are the fundamental mode and the 2BA mode, which are well separated for \mathbf{H} parallel to the nanodisk rows and very close for \mathbf{H} perpendicular to them (with a contribution of the 4BA mode in the latter case).

IV. CONCLUSIONS

In summary, we have presented a detailed comparison of experimental and numerical simulation results for the quasistatic magnetization reversal and spin-wave excitation spectra in hexagonally ordered arrays of magnetic nanodisks. The highly ordered arrays with the hexagonal lattice constant of about $a = 390$ nm have been patterned using the ENSL of a 20-nm-thick $\text{Ni}_{80}\text{Fe}_{20}$ film. We have compared the quasistatic and dynamic behavior of two array kinds: (i) array with the edge-to-edge interdisk separation $d_{\text{cp}} = 65$ nm (close-packed or *cp* array) and (ii) array with $d_{\text{ucp}} = 20$ nm (ultraclosed-packed or *ucp* array).

Hysteresis loops measured using the MOKE have shown that for both arrays the quasistatic reversal of the nanodisks magnetization proceeds via the vortex formation (in approximately zero field) and the subsequent vortex expulsion (in negative fields about several hundred Oersted). Vortex formation and expulsion fields depend on the interdisk edge-to-edge separation, i.e., they are different for *cp* and *ucp*

arrays. However, for the given array kind, both critical fields are nearly independent on the in-plane direction of the external field. For the vortex expulsion field, this independence can be explained by the fact that vortices form a nearly closed magnetization configuration, so the magnetodipolar interaction between different disks is relatively weak even in the *ucp* array. Extensive micromagnetic simulations with the input material parameters determined from the continuous film measurements have demonstrated that hysteresis loops can be reproduced quantitatively only under the assumption that the magnetization of nanodisks is significantly reduced in the narrow region near the nanodisk edges. Such a reduction might be due to the patterning process during the array production.

Spin-wave excitation spectra for the *cp* array, obtained by both the BLS and AESWS, are also isotropic with respect to the in-plane external field direction. In contrast, excitation spectra for the *ucp* array demonstrate significant in-plane anisotropy when the direction of the applied field is changed. Systematic numerical studies of the *ucp*-system eigenmodes (carried out by full-scale micromagnetic simulations and the DMM) have been performed for the external field directed along the two main symmetry axes of the hexagonal lattice. Simulations have revealed that the principal differences between the spin-wave spectra for these two cases are due to two reasons. First, the EM for one of these cases (field directed along the nanodisks rows) is absent due to the nearly complete cancelation of the self-demagnetizing field of a nanodisk by the stray field of its nearest neighbors. Second, the spatial power distributions of modes concentrated in central regions of the nanodisks (bulk modes) also strongly depend on the external field orientation due to the anisotropy of the magnetodipolar interaction between the disks in the *ucp* array. Comparing simulation results with the experimental spectra, we could unambiguously identify all experimentally observed modes.

A reliable identification and classification of observed modes and determination of material parameters are mandatory prerequisites for any generalization using either analytical or numerical methods. Therefore, the thorough presentation of

the data set in this paper can serve as a useful starting point for application and mutual comparison of the various theories in magnonics. We also expect that our results will stimulate in the nearest future the execution of further studies with a similar degree of rigor, creating the critical mass required to achieve a comprehensive understanding of the high-frequency magnetodynamics in arrays of nanoelements.

ACKNOWLEDGMENTS

The authors greatly acknowledge the European Community's Seventh Framework Programme (FP7/2007-2013) under Grant Agreement No. 228673 (MAGNONICS) and from EPSRC of the UK under Project No. EP/E055087/1 and also MIUR under PRIN 2010-2011 "DyNanoMag," Project No. 2010ECA8P3.

*Corresponding author: db@innovoent-jena.de

- ¹A. G. Gurevich and G. A. Melkov, *Magnetization Oscillations and Waves* (Chem. Rubber Corp., Boca Raton, 1996).
- ²C. Mathieu, J. Jorzick, A. Frank, S. O. Demokritov, A. N. Slavin, B. Hillebrands, B. Bartenlian, C. Chappert, D. Decanini, F. Rousseaux, and E. Cambril, *Phys. Rev. Lett.* **81**, 3968 (1998).
- ³Y. Roussigné, S. M. Chérif, C. Dugautier, and P. Moch, *Phys. Rev. B* **63**, 134429 (2001).
- ⁴G. Gubbiotti, G. Carlotti, R. Zivieri, F. Nizzoli, T. Okuno, and T. Shinjo, *J. Appl. Phys.* **93**, 7607 (2003).
- ⁵J. Jorzick, S. O. Demokritov, B. Hillebrands, M. Bailleul, C. Fermon, K. Y. Guslienko, A. N. Slavin, D. V. Berkov, and N. L. Gorn, *Phys. Rev. Lett.* **88**, 047204 (2002).
- ⁶J. P. Park, P. Eames, D. M. Engebretson, J. Berezovsky, and P. A. Crowell, *Phys. Rev. Lett.* **89**, 277201 (2002).
- ⁷A. Barman, V. V. Kruglyak, R. J. Hicken, J. M. Rowe, A. Kundrotaite, J. Scott, and M. Rahman, *Phys. Rev. B* **69**, 174426 (2004).
- ⁸M. Bailleul, R. Höllinger, K. Perzlmaier, and C. Fermon, *Phys. Rev. B* **76**, 224401 (2007).
- ⁹G. Gubbiotti, P. Candeloro, L. Businaro, E. Di Fabrizio, A. Gerardino, R. Zivieri, M. Conti, and G. Carlotti, *J. Appl. Phys.* **93**, 7595 (2003).
- ¹⁰M. Pardavi-Horvath, C. A. Ross, and R. D. McMichael, *IEEE Trans. Magn.* **41**, 3601 (2005).
- ¹¹V. V. Kruglyak, P. S. Keatley, R. J. Hicken, J. R. Childress, and J. A. Katine, *Phys. Rev. B* **75**, 024407 (2007).
- ¹²S. O. Demokritov (ed.), *Spin Wave Confinement* (Pan Stanford Publishing, Singapore, 2009).
- ¹³S. A. Nikitov, P. Tailhades, and C. S. Tsai, *J. Magn. Magn. Mater.* **236**, 320 (2001).
- ¹⁴G. Gubbiotti, S. Tacchi, M. Madami, G. Carlotti, A. O. Adeyeye, and M. Kostylev, *J. Phys. D: Appl. Phys.* **43**, 264003 (2010).
- ¹⁵S. Tacchi, M. Madami, G. Gubbiotti, G. Carlotti, S. Goolaup, A. O. Adeyeye, N. Singh, and M. P. Kostylev, *Phys. Rev. B* **82**, 184408 (2010).
- ¹⁶Z. K. Wang, V. L. Zhang, H. S. Lim, S. C. Ng, M. H. Kuok, S. Jain, and A. O. Adeyeye, *ACS Nano* **4**, 643 (2010).
- ¹⁷J. Topp, D. Heitmann, M. P. Kostylev, and D. Grundler, *Phys. Rev. Lett.* **104**, 207205 (2010); J. Topp, S. Mendach, D. Heitmann, M. Kostylev, and D. Grundler, *Phys. Rev. B* **84**, 214413 (2011).
- ¹⁸A. Y. Galkin, B. A. Ivanov, and C. E. Zaspel, *Phys. Rev. B* **74**, 144419 (2006).
- ¹⁹P. S. Keatley, V. V. Kruglyak, A. Neudert, E. A. Galaktionov, R. J. Hicken, J. R. Childress, and J. A. Katine, *Phys. Rev. B* **78**, 214412 (2008).
- ²⁰S. Tacchi, M. Madami, G. Gubbiotti, G. Carlotti, H. Tanigawa, T. Ono, and M. P. Kostylev, *Phys. Rev. B* **82**, 024401 (2010).
- ²¹S. Tacchi, F. Montoncello, M. Madami, G. Gubbiotti, G. Carlotti, L. Giovannini, R. Zivieri, F. Nizzoli, S. Jain, A. O. Adeyeye, and N. Singh, *Phys. Rev. Lett.* **107**, 127204 (2011).
- ²²S. Neusser, G. Duerr, S. Tacchi, M. Madami, M. L. Sokolovskyy, G. Gubbiotti, M. Krawczyk, and D. Grundler, *Phys. Rev. B* **84**, 094454 (2011).
- ²³B. Lenk, H. Ulrichs, F. Garbs, and M. Münzenberg, *Phys. Rep.* **507**, 107 (2011), and references therein.
- ²⁴V. V. Kruglyak and R. J. Hicken, *J. Magn. Magn. Mater.* **306**, 191 (2006); V. V. Kruglyak, S. O. Demokritov, and D. Grundler, *J. Phys. D: Appl. Phys.* **43**, 264001 (2010), and references therein.
- ²⁵J. Ding, M. Kostylev, and A. O. Adeyeye, *Appl. Phys. Lett.* **100**, 073114 (2012).
- ²⁶S. V. Vasiliev, V. V. Kruglyak, M. L. Sokolovskii, and A. N. Kuchko, *J. Appl. Phys.* **101**, 113919 (2007); A. Khitun, M. Q. Bao, and K. L. Wang, *J. Phys. D: Appl. Phys.* **43**, 264005 (2010), and references therein.
- ²⁷V. V. Kruglyak, P. S. Keatley, A. Neudert, R. J. Hicken, J. R. Childress, and J. A. Katine, *Phys. Rev. Lett.* **104**, 027201 (2010); R. V. Mikhaylovskiy, E. Hendry, and V. V. Kruglyak, *Phys. Rev. B* **82**, 195446 (2010); S. Neusser, H. G. Bauer, G. Duerr, R. Huber, S. Mamica, G. Woltersdorf, M. Krawczyk, C. H. Back, and D. Grundler, *ibid.* **84**, 184411 (2011); V. V. Kruglyak, M. Dvornik, R. V. Mikhaylovskiy, O. Dmytriiev, G. Gubbiotti, S. Tacchi, M. Madami, G. Carlotti, F. Montoncello, L. Giovannini, R. Zivieri, J. W. Klos, M. L. Sokolovskyy, S. Mamica, M. Krawczyk, M. Okuda, J. C. Eloi, S. Ward Jones, W. Schwarzacher, T. Schwarze, F. Brandl, D. Grundler, D. V. Berkov, E. Semenova, and N. Gorn, "Magnonic Metamaterials," in *Metamaterial* (InTech, Rijeka, 2012).
- ²⁸J. W. Lau and J. M. Shaw, *J. Phys. D: Appl. Phys.* **44**, 303001 (2011).
- ²⁹S. M. Weekes, F. Y. Ogrin, W. A. Murray, and P. S. Keatley, *Langmuir* **23**, 1057 (2007); E. Sirotkin and F. Y. Ogrin, *IEEE Trans. Magn.* **46**, 1840 (2010).
- ³⁰M. Kostylev, R. Magaraggia, F. Y. Ogrin, E. Sirotkin, V. F. Mescheryakov, N. Ross, and R. L. Stamps, *IEEE Trans. Magn.* **44**, 2741 (2008).
- ³¹N. Ross, M. Kostylev, and R. L. Stamps, *J. Appl. Phys.* **109**, 013906 (2011).
- ³²S. Tacchi, M. Madami, G. Gubbiotti, G. Carlotti, H. Tanigawa, T. Ono, and M. P. Kostylev, *Phys. Rev. B* **82**, 024401 (2010).
- ³³B. Rana, D. Kumar, S. Barman, S. Pal, R. Mandal, Y. Fukuma, Y. Otani, S. Sugimoto, and A. Barman, *J. Appl. Phys.* **111**, 07D503 (2012).
- ³⁴S. Jung, B. Watkins, L. DeLong, J. B. Ketterson, and V. Chandrasekhar, *Phys. Rev. B* **66**, 132401 (2002).

- ³⁵I. P. Nevirkovets, O. Chernyashevskyy, J. B. Ketterson, V. Metlushko, and B. K. Sarma, *J. Appl. Phys.* **104**, 063920 (2008).
- ³⁶A. Vogel, A. Drews, Mi-Young Im, P. Fischer, and Guido Meier, *IEEE Trans. Magn.* **47**, 1610 (2011).
- ³⁷C. Mathieu, C. Hartmann, M. Bauer, O. Buettner, S. Riedling, B. Roos, S. O. Demokritov, B. Hillebrands, B. Bartenlian, C. Chappert, D. Decanini, F. Rousseaux, E. Cambril, A. Müller, B. Hoffmann, and U. Hartmann, *Appl. Phys. Lett.* **70**, 2912 (1997).
- ³⁸G. Gubbiotti, M. Madami, S. Tacchi, G. Carlotti, G. Socino, and T. Okuno, *Surf. Sci.* **600**, 4143 (2006).
- ³⁹H. Ulrichs, V. E. Demidov, Sergej O. Demokritov, A. V. Ognev, M. E. Stebly, L. A. Chebotkevich, and A. S. Samardak, *Phys. Rev. B* **83**, 184403 (2011).
- ⁴⁰E. Tartakovskaya, W. Kreuzpaintner, and A. Schreyer, *J. Appl. Phys.* **103**, 023913 (2008).
- ⁴¹M. Wolf, C. Patschreck, R. Schäfer, I. Mönch, L. Schultz, and J. McCord, *J. Magn. Magn. Mater.* **323**, 1703 (2011).
- ⁴²R. Verba, G. Melkov, V. Tiberkevich, and A. Slavin, *Phys. Rev. B* **85**, 014427 (2012).
- ⁴³A. A. Awad, G. R. Aranda, D. Dieleman, K. Y. Guslienko, G. N. Kakazei, B. A. Ivanov, and F. G. Aliev, *Appl. Phys. Lett.* **97**, 132501 (2010).
- ⁴⁴M. Grimsditch, L. Giovannini, F. Montoncello, F. Nizzoli, G. K. Leaf, and H. G. Kaper, *Phys. Rev. B* **70**, 054409 (2004).
- ⁴⁵L. Giovannini, F. Montoncello, and F. Nizzoli, *Phys. Rev. B* **75**, 024416 (2007).
- ⁴⁶V. V. Kruglyak, A. Barman, R. J. Hicken, J. R. Childress, and J. A. Katine, *Phys. Rev. B* **71**, 220409 (2005).
- ⁴⁷G. Gubbiotti, M. Madami, S. Tacchi, G. Carlotti, and T. Okuno, *J. Appl. Phys.* **99**, 08C701 (2006).
- ⁴⁸C. C. Dantas, *Physica E* **44**, 675 (2011).
- ⁴⁹V. N. Krivoruchko and A. I. Marchenko, *J. Appl. Phys.* **109**, 083912 (2011).
- ⁵⁰E. Sirotkin, J. D. Apweiler, and F. Y. Ogrin, *Langmuir* **26**, 10677 (2010).
- ⁵¹S. Neusser, G. Durr, H. G. Bauer, S. Tacchi, M. Madami, G. Woltersdorf, G. Gubbiotti, C. H. Back, and D. Grundler, *Phys. Rev. Lett.* **105**, 067208 (2010).
- ⁵²J. Podbielski, F. Giesen, M. Berginski, N. Hoyer, and D. Grundler, *Superlattices Microstruct.* **37**, 341 (2005).
- ⁵³G. Carlotti and G. Gubbiotti, *La Rivista del Nuovo Cimento* **22**, 1 (1999).
- ⁵⁴D. V. Berkov and N. L. Gorn, MicroMagus—package for micro-magnetic simulations, <http://www.micromagus.de>.
- ⁵⁵B. Hillebrands, *Phys. Rev. B* **41**, 530 (1990).
- ⁵⁶K. Yamamoto and M. Kitada, *J. Mater. Sci.: Mater. Electron.* **7**, 455 (1996).
- ⁵⁷R. W. O'Neill and S. McVitie, *J. Phys.: Conf. Series* **26**, 187 (2006).
- ⁵⁸R. P. Cowburn, D. K. Koltsov, A. O. Adeyeye, M. E. Welland, and D. M. Tricker, *Phys. Rev. Lett.* **83**, 1042 (1999).
- ⁵⁹A. Fernandez and C. J. Cerjan, *J. Appl. Phys.* **87**, 1395 (2000).
- ⁶⁰S. P. Li, M. Natali, A. Lebib, A. Pepin, Y. Chen, and Y. B. Xu, *J. Magn. Magn. Mater.* **241**, 447 (2002).
- ⁶¹M. Natali, A. Popa, U. Ebels, Y. Chen, S. Li, and M. E. Welland, *J. Appl. Phys.* **96**, 4334 (2004).
- ⁶²M. Heumann, T. Uhlig, and J. Zweck, *Phys. Rev. Lett.* **94**, 077202 (2005).
- ⁶³C. Redondo, B. Sierra, S. Moralejo, and F. Castano, *J. Magn. Magn. Mater.* **322**, 1969 (2010).
- ⁶⁴X. Zhu, P. Grütter, V. Metlushko, and B. Ilic, *Appl. Phys. Lett.* **80**, 4789 (2002).
- ⁶⁵M. Natali, A. Lebib, Y. Chen, I. L. Prejbeanu, and K. Ounadjela, *J. Appl. Phys.* **91**, 7041 (2002).
- ⁶⁶R. D. McMichael and B. B. Maranville, *Phys. Rev. B* **74**, 024424 (2006).
- ⁶⁷G. N. Kakazei, Y. G. Pogorelov, M. D. Costa, T. Mewes, P. E. Wigen, P. C. Hammel, V. O. Golub, T. Okuno, and V. Novosad, *Phys. Rev. B* **74**, 060406 (2006).
- ⁶⁸A. Hubert and R. Schäfer, *Magnetic Domains—The Analysis of Magnetic Microstructures* (Springer-Verlag, Berlin, 1998).
- ⁶⁹D. Goll, G. Schütz, and H. Kronmüller, *Phys. Rev. B* **67**, 094414 (2003).
- ⁷⁰F. Montoncello, L. Giovannini, F. Nizzoli, H. Tanigawa, T. Ono, G. Gubbiotti, M. Madami, S. Tacchi, and G. Carlotti, *Phys. Rev. B* **78**, 104421 (2008); F. Montoncello, L. Giovannini, F. Nizzoli, P. Vavassori, M. Grimsditch, T. Ono, G. Gubbiotti, S. Tacchi, and G. Carlotti, *ibid.* **76**, 024426 (2007).
- ⁷¹F. Montoncello, L. Giovannini, F. Nizzoli, P. Vavassori, and M. Grimsditch, *Phys. Rev. B* **77**, 214402 (2008).
- ⁷²C. Bayer, J. Jorzick, B. Hillebrands, S. O. Demokritov, R. Kouba, R. Bozinoski, A. N. Slavin, K. Guslienko, D. V. Berkov, N. L. Gorn, and M. P. Kostylev, *Phys. Rev. B* **72**, 064427 (2005).
- ⁷³F. Montoncello, L. Giovannini, and F. Nizzoli, *J. Appl. Phys.* **103**, 083910 (2008).
- ⁷⁴G. Gubbiotti, M. Conti, G. Carlotti, P. Candeloro, E. Di Fabrizio, K. Y. Guslienko, A. Andre, C. Bayer, and A. N. Slavin, *J. Phys.: Condens. Matter* **16**, 7709 (2004).
- ⁷⁵M. Grimsditch, L. Giovannini, F. Montoncello, F. Nizzoli, G. Leaf, H. Kaper, and D. Karpeev, *Physica B* **354**, 266 (2004).
- ⁷⁶M. Dvornik, P. V. Bondarenko, B. A. Ivanov, and V. V. Kruglyak, *J. Appl. Phys.* **109**, 07B912 (2011).